The Development and Requirements of a Body Force Database from Two-Dimensional and Streamline Curvature Calculations

by

Thomas K. Walker III

S.B. Aerospace Engineering
Massachusetts Institute of Technology, 2006

Submitted to the Department of Aeronautics and Astronautics
in partial fulfillment of the requirements for the degree of

Master of Science in Aeronautics and Astronautics

at the

MASSACHUSETTS INSTITUTE OF TECHNOLOGY

February 2009

Author . . . . . .
Department of Aeronautics and Astronautics
September 11, 2009

Certified by . . . . . .
Edward Greitzer
H.N. Slater Professor of Aeronautics and Astronautics
Thesis Supervisor

Certified by . . . . . .
Choon Sooi Tan
Senior Research Engineer
Thesis Supervisor

Accepted by . . . . . .
David L. Darmofal
Associate Department Head
Chair, Committee on Graduate Students

The Development and Requirements of a Body Force Database from Two-Dimensional and Streamline Curvature Calculations

by

Thomas K. Walker III

Submitted to the Department of Aeronautics and Astronautics
on September 11, 2009, in partial fulfillment of the
requirements for the degree of
Master of Science in Aeronautics and Astronautics

Abstract

This thesis presents a methodology for development of a body force database, from design conditions to flows below the stall point, for compressor stability analysis. The methodology is based on two-dimensional blade element calculations and a streamline curvature procedure to calculate the axisymmetric flow, although it can be extended to use three-dimensional calculations where available. The methodology is demonstrated by assembling the body force database and using it for a stability calculation. The connection between the stall onset behavior and the body forces near and below the stall point is established through a sensitivity assessment of the radial and axial distribution of the body forces. Comparisons are made with stall onset data obtained in a single stage axial compressor. Capturing the axial component of the body force is found to be key element in estimation of the stall point and stall inception type.

Thesis Supervisor: Edward Greitzer
Title: H.N. Slater Professor of Aeronautics and Astronautics

Thesis Supervisor: Choon Sooi Tan
Title: Senior Research Engineer

[THIS PAGE IS INTENTIONALLY LEFT BLANK]

Acknowledgments

Firstly, I would like to thank MHI for sponsoring this research program and hiring me as an employee beginning this fall. Specifically, I am grateful to Sumiu Uchida, for his hard work on the project and helping me with the transition to Japan. I'm looking forward to working at MHI.

I am indebted to the entire MIT/MHI team: Prof. Greitzer, Dr. Tan, Prof. Spakovsky, Dr. Adamczyk, Dr. Yifang Gong, Prof. Jun Li, Prof. Qiushi Li, Georg Reichstein, and Amish Patel. My advisors, Prof. Greitzer and Dr. Tan, always pushed me to work hard and become a better student and researcher. I am a better engineer now than I was two years ago because of their knowledge, advice, and support. I thank Prof. Spakovsky and Dr. Adamczyk for their keen insight during the weekly meetings which many times led me to solutions I could not see. And finally, I thank the rest of the team for all of their hard work in making this project possible.

I would also like to thank all my friends at MIT and the GTL whom I have not already mentioned. George Kiwada for sticking with me through the tough times on the project. Darr Tarr for teaching me how to ski. Danny Zayas and Alberto Gayon for being such great roommates. And all others who have helped me through these years at MIT.

Finally, I would like thank my family. Without their loving support and guidance, I doubt I would have made it though my time at MIT.

Contents

List of Figures

List of Tables

Chapter 1

Introduction

1.1 Introduction

Stability has been of interest to compressor designers since the advent of the gas turbine engine. Designing a compressor with adequate stall margin to avoid rotating stall or surge is a basic requirement. At the present, correlations of experimental data are used to determine the stall point, sometimes leading to surprises later in development. An accurate predictive stall methodology would allow designers to determine the stall margin during the design phase and avoid such a surprise.

The overall goal of this project, for which the present thesis is only a part, is to develop such a methodology based on recent advancements in knowledge of compressor behavior. Two examples are the work of Gong(4), who developed a stability model based on a body force representation of the compressor and showed that his model was able to capture the two routes to stall, spike and modal stall inception, and Kiwada(8), who developed a method to extract this force from three-dimensional calculations. The work discussed here addresses the description of the body force database for the wide range of flow conditions above and below the stall point.

1.2 Background

1.2.1 Rotating Stall and Surge

There are two types of compressor instabilities as sketched in Figure 1-1. The diagram on the left shows surge, the lowest order disturbance, with basically planar oscillations. The

diagram on the right shows rotating stall, a higher order disturbance in which regions of low flow rotate around the annulus at 15% -50% of the rotor revolution speed(1) depending on geometry.

There two types of rotating stall, full-span rotating stall where one large stall cell blocks the entire span throughout the compressor and part span rotating stall where one to several of smaller stall cells are present in one part of the span(4). In many cases, rotating stall leads into surge.

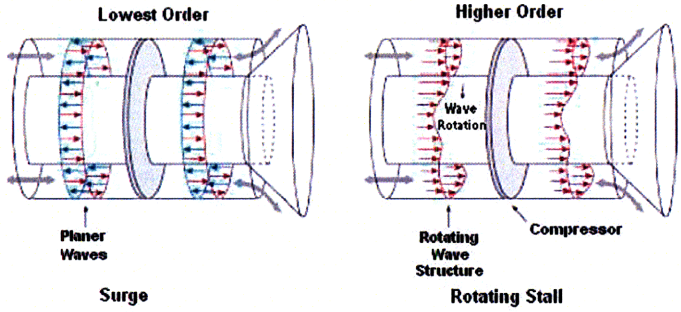

Figure 1-1: Example of the two final forms of compressor instability surge and rotating stall.

1.2.2 Rotating Stall Inception

The goal of this project is to put in place a methodology for accurate prediction of the flow coefficient at which rotating stall occurs. There are two types of rotating stall inception. The first is modal, or long wavelength, inception. The features of this type are that the length scale is on the order of the circumference of the compressor, and the initial amplitude small, with the process being an example of linear instability. Tens of rotor revolutions are needed for modes to grow (exponentially) into a mature rotating stall cell(1).

The second type is spike instability. Features of spikes are that the length scale is on the order of two or three blade passages, and the initial amplitude of which the disturbance is seen is large(1). Spike instability do not appear to be a linear process. As shown in the leftmost plot in Figure 1-2(a), modal stall if found if the peak(zero slope) of the characteristic occurs before the critical incidence, defined as the incidence where the rotor flow breaks down. If this incidence is not met before the peak of the curve, then rotating stall will

slowly develop through modes. In the right plot of Figure 1-2(a), there is an example of spike stall. In this case, the critical incidence is reached on the negatively-sloped side of the characteristic ans spike stall occurs, with the stall developing rapidly in about 2-3 rotor revolutions(1).

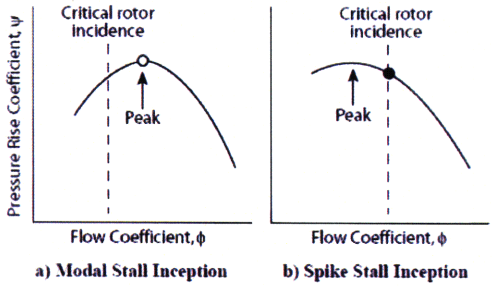

(a) Effect of critical rotor incidence and characteristic slope on stall inception type

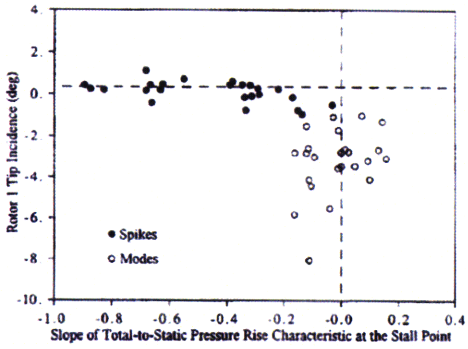

(b) Experimental verification of characteristic slope hypothesis

Figure 1-2: Diagram showing the type of stall inception and its relation to the slope of the characteristic(1).

Camp and Day(1) showed (Figure 1-2(b)) that stalls occurring on the negatively-sloped side of the characteristic are spike stall whereas if the slope is near zero when the compressor stalls it is modal stall. For the compressor examined here, experimental data indicates that spike stall inception occurs.

1.2.3 Body Forces

Compressor stability cannot be determined by localized single blade row calculations but to carry out detailed three-dimensional Navier-Stokes flow calculations for the whole machine would take an unreasonable amount of time. The approach here is to replace the blades with body force to reduce the computational requirements(12). To do this a accurate body force description is needed.

The basic idea is that the blade's effect on the fluid is represented by the body force, which can be extracted from Navier-Stokes computations. The relation between the flow field and the body force is described by the governing equations. For reference, these are included in Appendix A.1.

Due to limited computational resources, past body force models focused on capturing

specific unsteady phenomena. Longely(10) used a time-accurate simulation and modeled the blade with a one-dimensional body force description to study long wavelength disturbances. Xu, Hynes, Denton(13) developed viscous bulk force model for three-dimensional simulations and combined it with an inviscid body force from an axisymmetric flow field, also to capture long wavelengths disturbances. These models either lack information in the radial direction(Longely) or details of the body force distribution(Xu, Hynes, Denton) limiting effectiveness in capturing short wavelength phenomena. Gong's(4) representation is able to capture modes and spikes.

The body force description is locally axisymmetric and averaged over a blade pitch in the theta direction. The body force does not include viscous terms which are handled in a different manner(4). The body force is expressed in terms of the fluxes F, G, H and source term S by equations such as Eqn. 1.1.

$$\frac{\partial}{\partial x}F + \frac{\partial}{\partial \theta}G + \frac{\partial}{\partial r}H = S \tag{1.1}$$

These represent the flux in each direction for a given cell in the domain. For example, F, which is made up of four terms, represents the flux of mass flow in the axial direction and the axial transfer of momentum in the axial, tangential, and radial directions. In our case, $\frac{\partial}{\partial \theta}G = 0$ because the solution is locally axisymmetric. The source term, S, contains the three components of the body force. The definition of these terms is given in Appendix A.2.

1.2.3.1 Body Force Estimation

Kiwada(8) developed a method to obtain the body force from three-dimensional Navier-Stokes solver, streamline curvature calculations, or two-dimensional calculations. Kiwada defines a control volume as in Figure 1-3 from leading to trailing edge. The blade forces are found by balancing the momentum flux through the control volume and the pressure forces on the surface of the control volume. In terms of Eqn. 1.1, the body force is extracted by equating the derivatives of F, G, and H to S and solving for the force. These variables are computed using the "blade force" averaging procedure developed by Kiwada(8), a momentum flux theta average of the three-dimensional flow field. This extraction procedure is applied throughout the domain resulting in complete description of the body force distribution

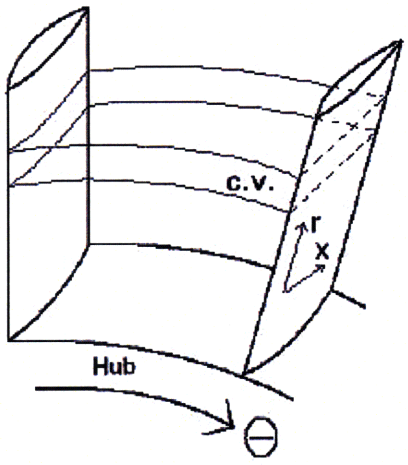

Figure 1-3: Example control volume used to extract the body forces(8).

1.2.3.2 Applying the Body Force to Predict Stall

It has been shown by Gong(4) and Xu, et al(13) that it is not necessary to resolve the details of the blade to blade unsteady flow for stall prediction. The body force, however, must to be linked to changes in the local flow. The quantity currently used is the local flow coefficient, ϕ_{local}.

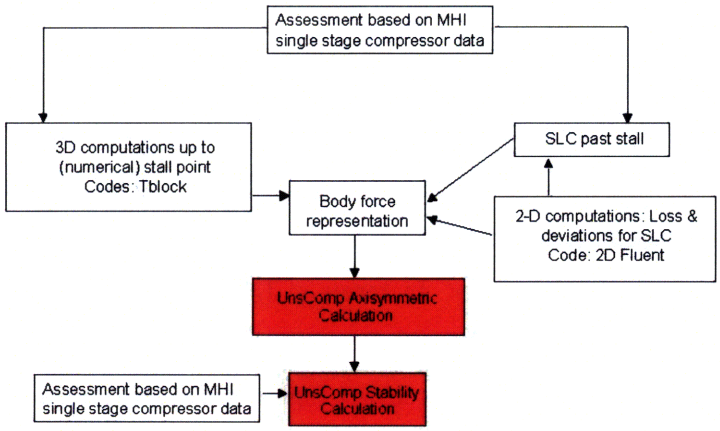

Figure 1-4: Flow Chart showing the path of the compressor stability research program.

1.3 Project Overview

In creating the stall prediction methodology beginning from the blade geometry an accurate body force model linked to the local flow coefficient must be extracted and used for a stability analysis. A flow chart outlines this process in Figure 1-4. The code used in this is UnsComp developed by Gong(4). The focus of this thesis is developing the body force representation as well as assessing the sensitivity of the unsteady results to the body forces.

1.4 Thesis Contributions

1) Estimation of body forces using two-dimensional viscous flow simulations plus streamline curvature calculations for flows from design to well below the stall point.

2) Establishment of a procedure to create a database that uses body forces extracted from a 3D Navier-Stokes solver from design to the stall point joined with the two-dimensional streamline curvature (2D/SLC) body force estimates.

3) Assessment of the unsteady behavior of the compressor using 2D/SLC body force estimates. Determination of the features of the body force description that are most important (the axial component) in determining the stall onset.

4) Demonstration of the end-to-end calculation (from geometry to instability onset) and comparison with single stage data which provide encouragement about the potential of the methodology for stall prediction.

1.5 Organization

This thesis is organized into three sections. Chapters 2-4 deal with the development and the calculations involved with preparing the body force from the 2D/SLC model for use in the stall simulation. Chapter 2 discusses the basic idea. Chapter 3 presents the a set of two-dimensional computations, and Chapter 4 discusses a set of streamline curvature calculations and discusses preparation of the body force database for use in UnsComp.

Chapter 5 develops an evaluation the stall prediction methodology for self-consistency..

Chapter 6 discusses the sensitivity of the stall inception to the features of body force.

Chapter 2

2D/SLC Model and Development of a Body Force Database

2.1 Requirements for Stall Prediction

To describe a blade row with the body force one must know the effect of the blade on the flow. Near design, there are many ways to obtain information about the flow field including two and three dimensional Navier-stokes solvers. For the present problems, however, it is not enough to know the effect of a blade near design. As shown in Figure 2-1, even if the background flow is on the negatively-sloped side of the characteristic a spike disturbance can access the stalled flow regime(4). Given that the response to an input disturbance determines the stall point and inception type, an accurate description of the compressor for a range of flow from design to reverse is required for the stall prediction model.

The requirement for use of UnsComp as a stall prediction tool is a body force database as a function of the local flow coefficient, defined as $\phi_{local} = \frac{V_{x_{local}}}{U_{local}}$ where $V_{x_{local}}$ is the velocity in any given cell and U_{local} is the rotor wheel speed at the corresponding radius. The database is in the form $f(x, r, \phi_{local})$, where f is the local body force for each cell. For reasons mentioned above, the body force database must contain information about the force at local flow coefficients from design to $-.2$. The goal is to have the body force database accurate enough to predict the stall point within 5% . To assess the requirements for accuracy of the body force, a sensitivity analysis of the stall point and stall inception type was performed. The results are shown later in this thesis.

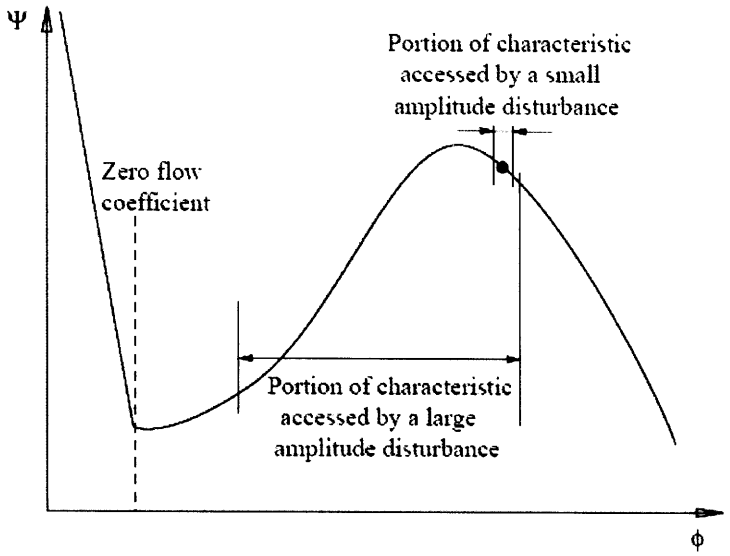

Figure 2-1: Effect of large amplitude short wavelength disturbances. Stalled flow is accessed by the spike even on the negatively sloped side of the characteristic(4).

2.2 Creating the Model

The methodology developed to meet these requirements, termed the 2D/SLC model, can be broken into three major parts. First, a two dimensional (steady flow) cascade calculation using the given geometry. Second, a streamline curvature computation with input flow angle and loss from the cascade calculations. Third, the distribution of the body force, extracted from the streamline curvature calculation, from the blade leading to trailing edge.

2.3 Development of a Body Force Database

Two body force are databases shown in Figure 2-2. The first is from the 2D/SLC estimate, $f(x, r, \phi_{overall_{SLC}})$, linked to ϕ_{local}. This database will be termed "the 2D/SLC body force database". The second is from a combination of $f(x, r, \phi_{overall_{SLC}})$ and $f(x, r, \phi_{overall_{3D}})$ linked to ϕ_{local}, where $f(x, r, \phi_{overall_{3D}})$ is extracted from a theta-average three dimensional flow field as given by Kiwada(8). The force from the three dimensional flow field is used where available (unstalled flow) and the force from streamline curvature is used for stalled flow. This database will be termed "the 3D/SLC body force database". This thesis developments the methodology to create the 3D/SLC body force database, however, all stability

calculations use the 2D/SLC body force database since the three dimensional flow field is not yet available.

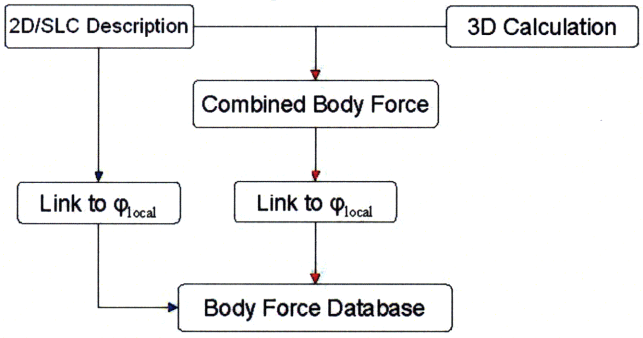

Figure 2-2: Flow chart describing the two different databases that can be created using the force estimates from the 2D/SLC procedure. The path depicting the 2D/SLC body force database is in blue and the 3D/SLC database in red.

2.4 2D/SLC Model

2.4.1 Two Dimensional Cascade Calculations

For a streamline curvature calculation to be performed, loss and flow angle must be calculated and input into the streamline curvature solver. To obtain the loss and deviation, two-dimensional calculations were done using FLUENT. The cascade geometry and the flow coefficient were the inputs. Calculations were run between $\Phi = 1$ and $\Phi = .4$ where $\Phi \equiv \frac{\phi}{\phi_{des}}$ and $\Phi_{stall} = .76$. The flow was computed at three radii (10%, 50%, 90% of span) so a radial distribution of the loss, deviation, and incidence could be input into streamline curvature.

The shortcoming of this approach is that 2D calculations can not capture flow features such as hub separation or tip leakage flow. For the present compressor, both of these features are important as the flow rate is decreased. Near design the flow over most of the blade behaves two dimensionally with little or no streamline curvature. However, near stall the blades operate locally at very different conditions (2) so a two dimensional steady flow solver by itself does not include all the relevant features.

2.4.2 Streamline Curvature Calculation

In their most basic form, streamline curvature codes solve for the position of the streamline in the xr plane using radial equilibrium and conservation of mass. If one knows flow angle and loss, a streamline curvature code(3) is capable of calculating the radial variations of from design to past the stall point. In the present procedure, the computed loss and deviation from the 2D calculation are input at the trailing edge of each blade. The body force can then be extracted from the flow field computed by the streamline curvature code. This procedure is termed here the SLC method.

The streamline curvature code currently being used only has leading and trailing edge nodes. The body force that is extracted is the total body force at each radius rather than $f(x, r, \phi_{local})$. This leaves the task of distributing this total body force along the chord, a process which will be discussed in a later section. Other limitations of the code used include the imposition of blockage at the trailing edge and the inability to calculate reverse flow.

2.4.3 Distribution of the Total Force Extracted from SLC

The streamline curvature body force must be distributed along the chord at each radius to satisfy the requirement that the force be in the form $f(x, r, \phi_{local})$. From experience, one might expect a distribution where most of the force is concentrated near the leading edge of the blade. The three-dimensional Navier-Stokers solvers give this distribution but they do not converge at or below stall. The method used for distributing the force along the chord was to use the force distributions extracted from the 2D cascade calculations and scale them to the total force at each radius obtained from the SLC flow field. The distributed force was then linked to ϕ_{local} creating the 2D/SLC body force database. The reason for distributing the body force in this way is that the 2D calculation is the only source of information regarding the flow past the stall point. It seems logical to apply the two-dimensional distribution to the total body force from SLC since the inputs were the loss and deviation computed from those calculations. An assessment of the influence of this distribution is given chapter 6.

2.5 Procedure for Developing the 3D/SLC Body Force Database

The most detailed flow solvers, with no assumptions other than for turbulence modeling, are three dimensional Navier-Stoker solvers and procedures have been developed to combine the body force extracted from these codes and the 2D/SLC body force database. Along the span of each blade, the flow coefficient at which the three dimensional flow field data is no longer available is determined. The body forces from the 2D/SLC method are used at lower flows, with the slope of the two force estimations matched to ensure a smooth transition between the forces computed by the two calculations. The combined body force was linked to ϕ_{local} creating the 3D/SLC body force database. However, this method has an additional layer of complexity since unsteady simulations, which can be time consuming, must be time averaged before they can be used with Gong's(4) steady axisymmetric body force methodology.

Chapter 3

2D Calculations and Body Force Extraction

This chapter details setting up and running the 2D Navier-Stokes calculation. Processing of the flow field is also discussed including extraction the body force distributions.

3.1 Flow Field Calculation

The geometry for this calculation is from a single stage test rig. For the two-dimensional estimate the flow in each blade row was calculated separately with one pitch in the circumferential direction, two chord lengths upstream, and four chord lengths downstream of the trailing edge to allow the flow to mix out. A grid study was done to determine a reasonable grid density that gave an accurate solution past the stall point. The turbulence model was the κ-ϵ model with enhanced wall treatment for more accurate resolution of the boundary layer. This is a standard model in FLUENT.

The calculation was run for a range of flow conditions from design to below stall. A case was considered converged if two conditions were met. The first condition was the maximum mass flow residual be less than 10^{-7} and the second that the change in static pressure at the inlet for one iteration be less than 1%. Three flow field variables(V_x,V_{y_rel}, and P) were extracted at the inlet and the exit of the domain for further processing.

3.1.1 2D Calculation Results

The conditions shown below are the rotor and stator flow fields at $\Phi = 1$, $\Phi = .761$, and $\Phi = .42$, conditions at design, the stall point, and low flow. Figure 3-1 shows the rotor and stator at design condition.

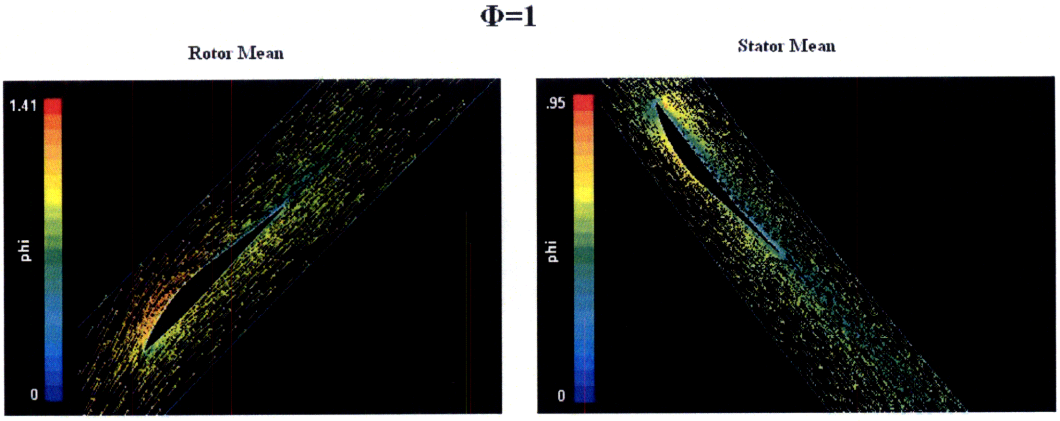

Figure 3-1: Flow field at the rotor and stator meanline at the design point. Phi is defined as the velocity at the inlet of the blade row divided by the local wheel speed.

At design the flow is well-behaved with small wakes. The wake is larger for the stator than it is for the rotor because the incidence angle is negative at this flow coefficient due to stator restaggering.

Near the stall point in Figure 3-2, the flow has begun to separate, most noticeably on the rotor. The rotor flow field separating around 50% chord is the cause for the pressure rise characteristic turning over. The stator flow is still attached at this condition.

Figure 3-3 shows the flow well past the measured stall point. The wake from the separation on the rotor nearly spans half a blade pitch and the separation point has also moved up to 30% of the chord. The stator flow field shows signs of separation, but not as severe as the rotor.

The flow field was also calculated at 10% span and 90% span to give information about the radial variation of the loss and flow angle as in Figure 3-4 and 3-5. The thickness and decreased stagger angle of the blade at the rotor hub are the reasons for the large region of separated flow (Figure 3-4) compared to the rotor mean radius. At the rotor tip (Figure 3-5), the flow field shows a large area of separation but smaller than the rotor mean. The

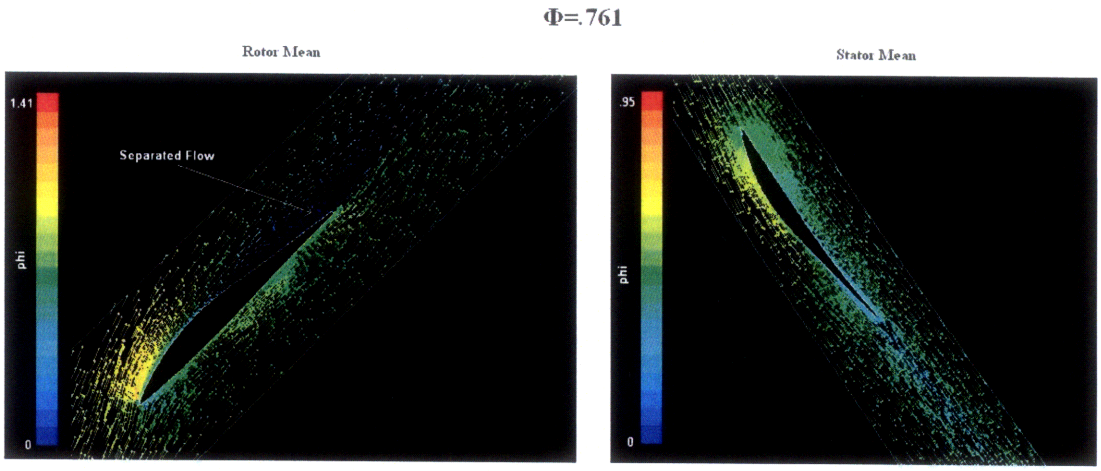

Figure 3-2: Flow field at the rotor and stator meanline at the stall point. Phi is defined as the velocity at the inlet of the blade row divided by the local wheel speed. Regions of separated flow are indicated on the figure.

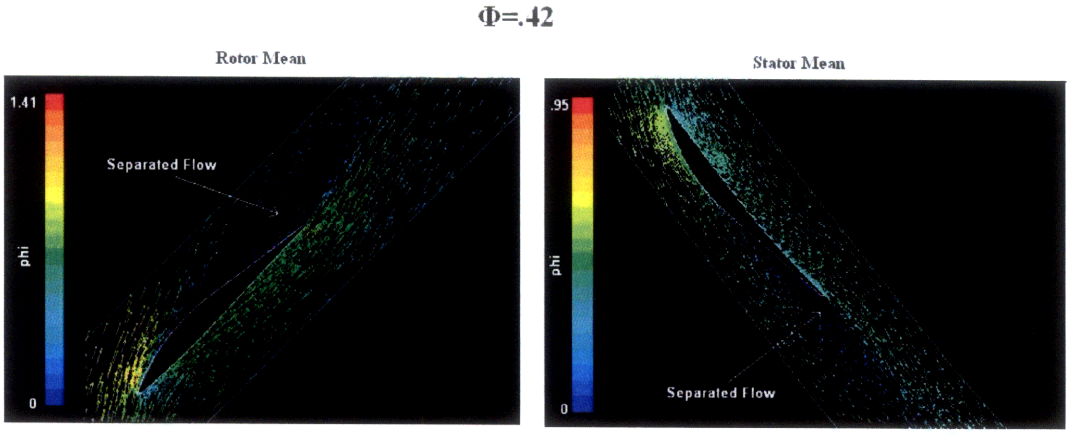

Figure 3-3: Flow field at the rotor and stator meanline well past the stall point. Phi is defined as the velocity at the inlet of the blade row divided by the local wheel speed. Regions of separated flow are indicated on the figure.

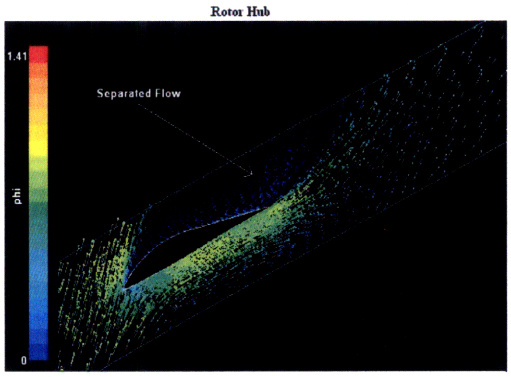

Figure 3-4: Flow field at the rotor hub well past the stall point. Phi is defined as the velocity at the inlet of the blade row divided by the local wheel speed. Regions of separated flow are indicated on the figure.

calculated flow at the rotor tip shows less separation than in test data since tip leakage flow was not calculated and, conversely, the flow at the rotor hub shows more separation since the streamlines would shift in that direction. The information needed for the streamline curvature calculation, the two-dimensional loss and deviation, is shown at the mean radius for each blade in Figures 3-6, 3-7, and 3-8.

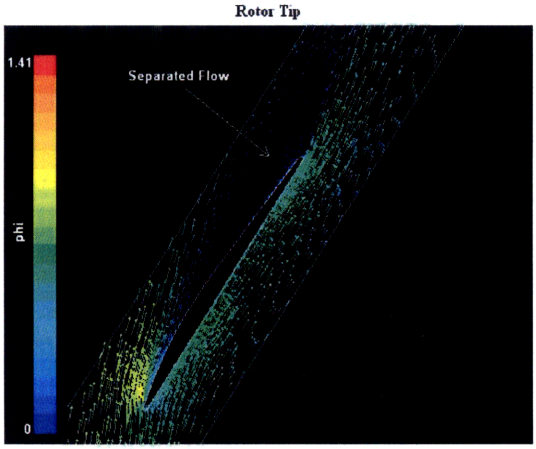

Figure 3-5: Flow field at the rotor tip well past the stall point. Phi is defined as the velocity at the inlet of the blade row divided by the local wheel speed. Regions of separated flow are indicated on the figure.

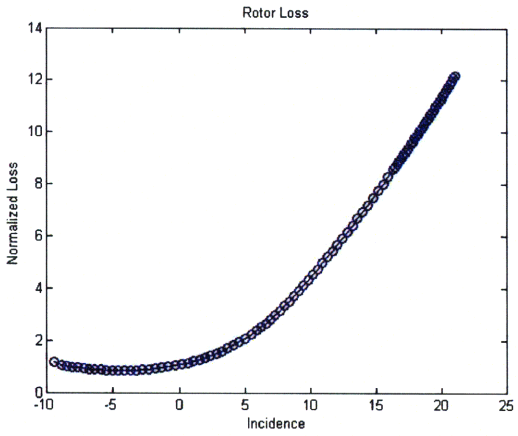

(a) Rotor Meanline Loss

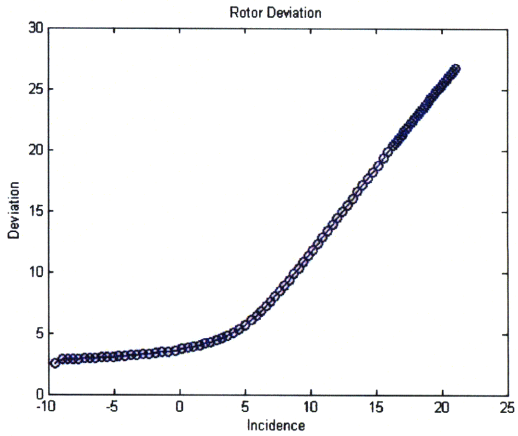

(b) Rotor Meanline Deviation

Figure 3-6: Rotor Meanline Loss and Deviation versus incidence. Normalized loss is loss/minimum loss.

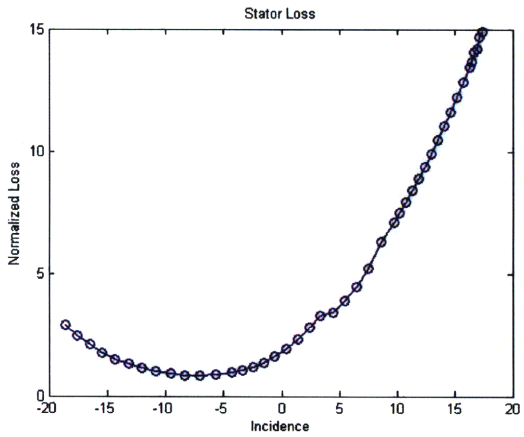

(a) Stator Meanline Loss

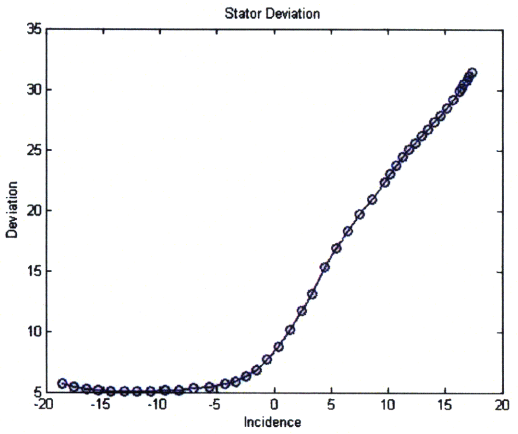

(b) Stator Meanline Deviation

Figure 3-7: Stator Meanline Loss and Deviation versus incidence. Normalized loss is loss/minimum loss.

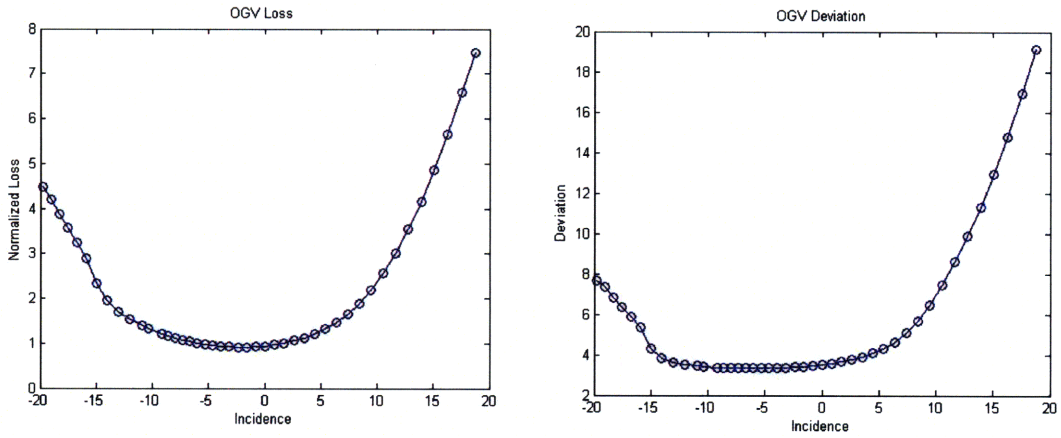

(a) OGV Meanline Loss

(b) OGV Meanline Deviation

Figure 3-8: OGV Meanline Loss and Deviation versus incidence. Normalized loss is loss/minimum loss.

3.2 Body Force Distribution

To distribute the total body force along the chord the two-dimensional calculations were used. The flow field variables (V_x, $V_{y_{rel}}$, P) were sampled in intervals 2% of chord (on average) with more samples taken near the leading edge to capture the steeper force gradients. Then the flux variables were calculated and theta averaged at each sample location. The fluxes and the pressure differences are normalized by the local dynamic head as described in Appendix B.

3.2.1 Force Distribution Results

Figures 3-1-3-11 show vectors of normalized body force along the chord of the rotor and stator. The force is normalized by the dynamic pressure based on wheel speed divided by the mean chord length. The normalization is consistent throughout this thesis.

At the rotor meanline near design the flow is attached (see Figure 3-1) giving the distribution in Figure 3-9 (a). At low flows shown in Figure 3-9 (b), the force is more concentrated towards the leading edge of the blade. As the flow coefficient is reduced further, Figure 3-10 (c), this trend continues. The trend in Figure 3-9 (a)-(c) is a consequence of the growing region of flow separation observed in Figures 3-2-3-5.

The rotor hub and tip show similar features (Figure 3-10). For the stator, near design, the leading edge shows reverse loading because of negative incidence. Figure 3-11 shows

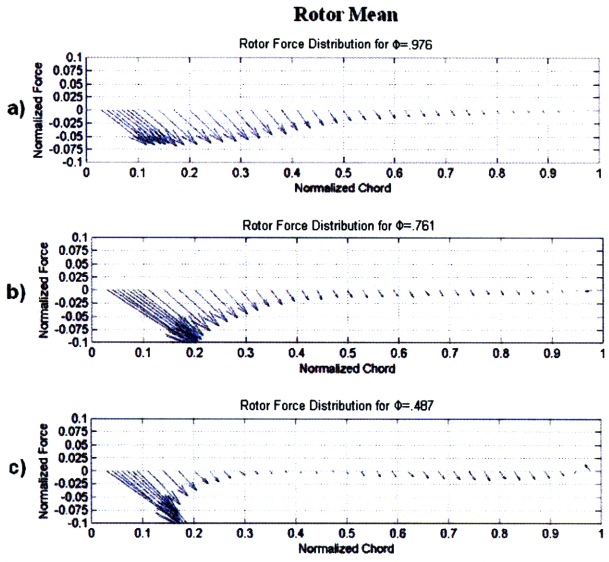

Figure 3-9: Distribution of force at the rotor meanline for three flow coefficients.

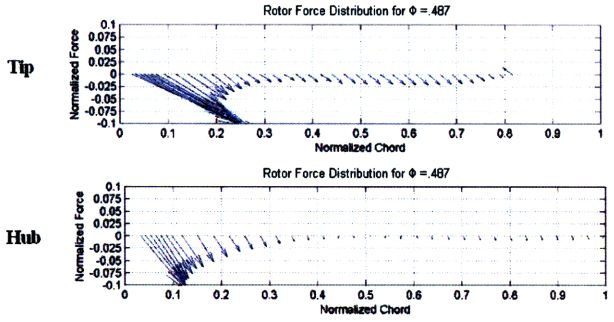

Figure 3-10: Distribution of force at the rotor hub and tip at ($\Phi = .487$)

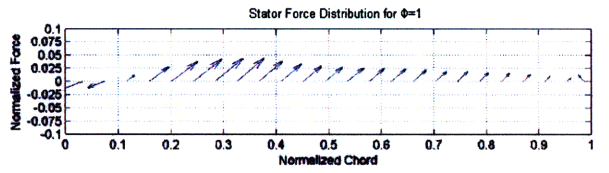

Figure 3-11: Distribution of force at the stator meanline showing reverse loading.

that in this region, 0% -10% of chord, the axial force is acting to retard the flow and the tangential force acting to turn the flow away from the blade. This is a consequence of a re-stagger that was carried out to relieve separation at the hub.

Chapter 4

SLC Calculations and the Body Force Database

Denton's streamline curvature code (SIMSLEQ) was used for streamline curvature calculations(3). Professor Q. Li(9) was responsible for modifications to the code and is given credit for his part in developing the modified SLC method. This chapter contains a brief description of the method and results from the calculations. The body force databases are created using the total body force from SLC and distributions from the 2D and 3D calculations.

4.1 Streamline Curvature Calculation

4.1.1 SLC Method

SIMSLEQ is a streamline curvature method with no nodes within the blade row. The loss and deviation are taken from the Fluent calculations as outlined in Figure 4-1. A one-dimensional velocity vector analysis which was done to find the incidence angle is used to get the 2D loss and deviation, the input into SIMSLEQ. As illustrated by "loop" shown in Figure 4-1, the incidence computed from the updated flow field from SIMSLEQ is used to re-interpolate the 2D curves until the solution converges.

4.1.2 SLC Results

In Figure 4-2 the calculations are compared to the overall total to static and blade static to static characteristics taken from the single stage rig. Shown is Ψ vs. Φ where $\Psi = \frac{\psi}{\psi_{design}}$.

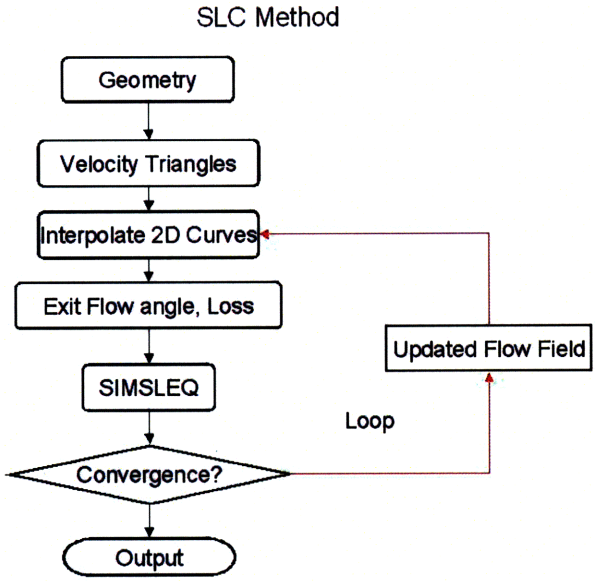

Figure 4-1: Flow chart detailing the SLC procedure(9).

This normalization is used through the thesis.

The slopes of the characteristics are similar near design, but there is larger pressure rise in the calculation than in the test data. The reason for the increased pressure rise is related mainly to differences in the rotor. The stall point is shown to be $\Phi_{overall} = .78$ in the calculation and experiment, however, the slope near stall of the characteristic and pressure rise coefficient are different. This is related to differences on the stator blade.

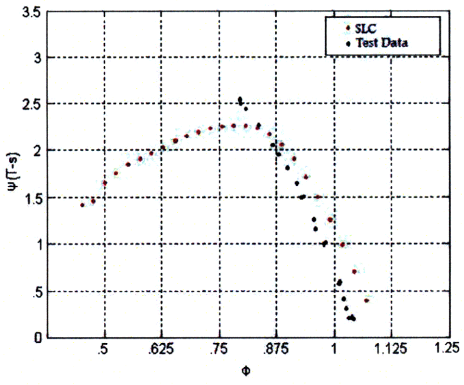

(a) Overall Characteristic $\psi(t-s)$ (9)

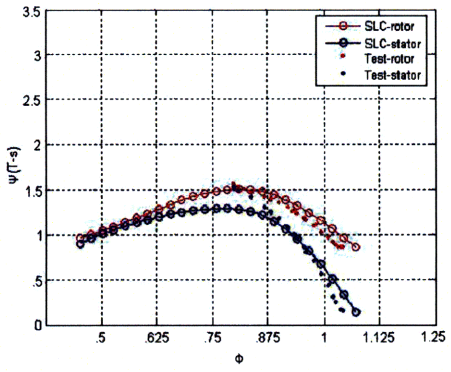

(b) Blade Characteristics $\psi(s-s)$ (9)

Figure 4-2: Characteristics for both the SLC calculation and test data.

The comparison of the radial loss distributions give more insight into the streamline curvature solution. Near design (Figure 4-3), the rotor data has higher loss than the calculations. Overall, the stator loss is matched reasonably well, although, the distribution along the span is different.

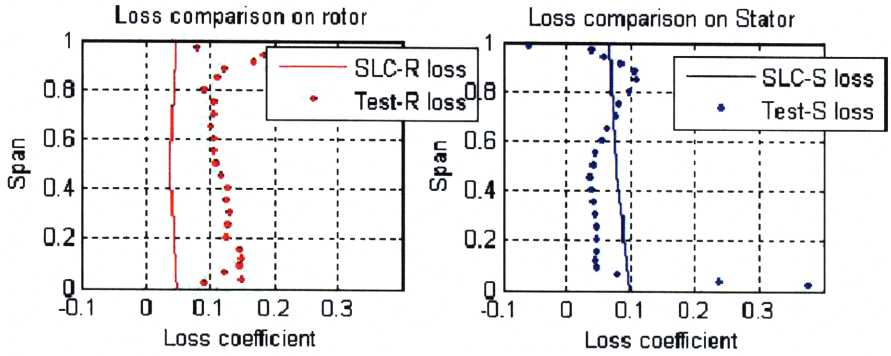

(a) Loss at Design $\psi(t-s)$ (9)

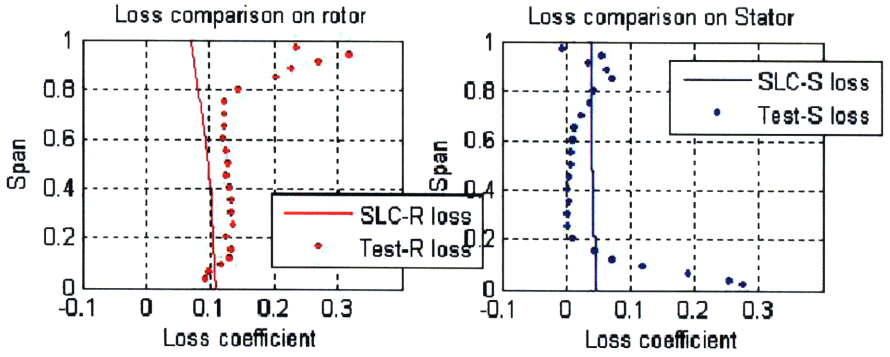

(b) Loss at near stall $\psi(s-s)$ (9)

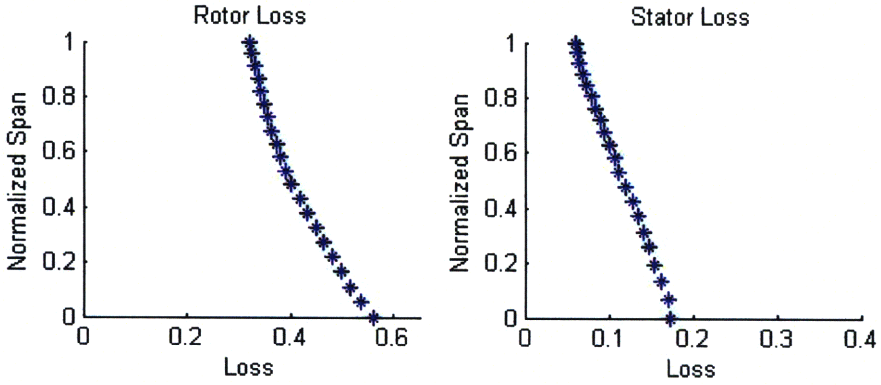

(c) Loss well past the stall point $\psi(s-s)$

Figure 4-3: Loss for the rotor and stator at $\Phi = .976$ and .809 for the SLC calculation and the MHI test data. In c), $\Phi = .476$, just the loss from SLC is shown.

Near stall, the data shows a strong effect of the tip leakage flow in the rotor and increased loss in the stator hub. Neither feature is captured by the calculation. Below the stall point, the calculation shows large losses at the rotor hub, corresponding to the rotor hub flow field seen in Figure 3-4. The stator hub also shows signs of separation, though not to the extent of the rotor.

To summarize, the overall characteristic compares well to the test characteristic near design but turns over earlier than data. The determination was that the SLC calculation captures enough of the flow features seen in the data to allow a useful examination of the while procedure.

4.2 Preparing the Body Force Database

The body force database is the input for UnsComp. It must be in the form $f(x, r, \phi_{local})$. Preparing the database includes extracting the total force from the SLC calculation and distributing the force along the chord of each blade row using the 2D force distributions. This section describes these steps and shows the resulting total body forces from SLC.

4.2.1 Extracting the Body Force

The original body force extraction code was written for use with a theta-averaged flow field from a 3D calculation(8). The streamline curvature code only has grid locations at the leading and trailing edges. To get the total body force at a radius in the original extraction procedure the force at each cell would have to be integrated along the chord, whereas with the streamline curvature code the total body force is directly output.

As with any streamline curvature code, the grid follows the streamlines. The body force procedure accounts for this by setting the flux of the velocity normal to the cell to zero. However, with only one cell over the blade chord numerical errors lead to small fluxes normal to the streamlines.

Figure 4-4 shows the computed axial and tangential body force at the meanline. Pressure is the flow variable that mainly determines the axial force (Eqn. A.4) so the F_x vs. ϕ curve looks much like the Ψ vs. Φ curve. The tangential force (Figure 4-5) is a measure of the flow turning. Flows beyond the stall point have large deviations. So there is decreased tangential force past the stall point.

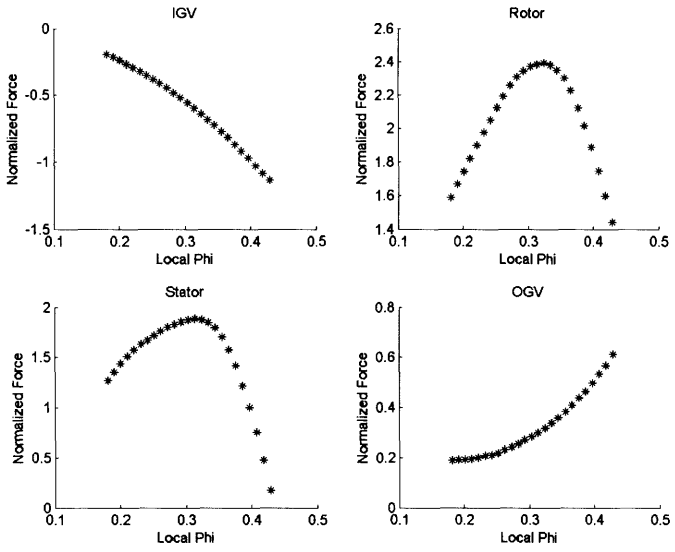

Figure 4-4: Axial body force at the meanline for each blade row from the SLC calculation. "Local Phi" is the ϕ at the shown radius.

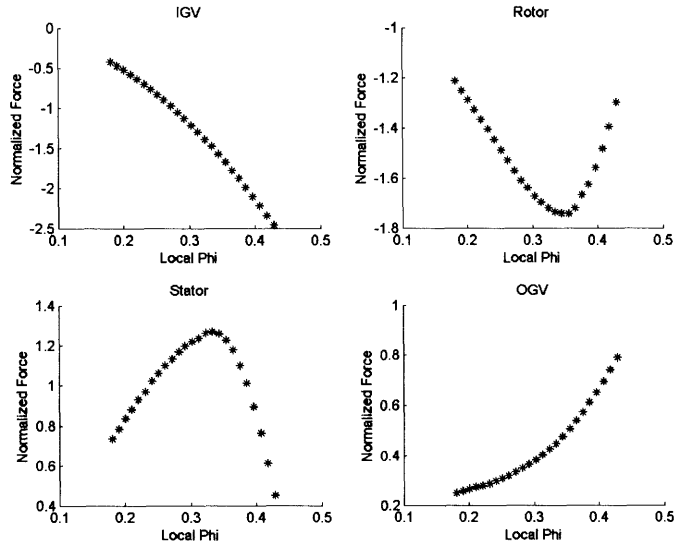

Figure 4-5: Tangential body force at the meanline for each blade row extracted from the SLC calculation. "Local Phi" is the ϕ at the shown radius.

4.2.2 Total Body Force Distribution

The final step in the 2D/SLC model is distributing the body force along the chord. Distributions from the Fluent calculations are sampled onto a grid along the blade and scaled so the total force is equal to that extracted from the streamline curvature calculation. The flow chart, Figure 4-6 outlines this procedure.

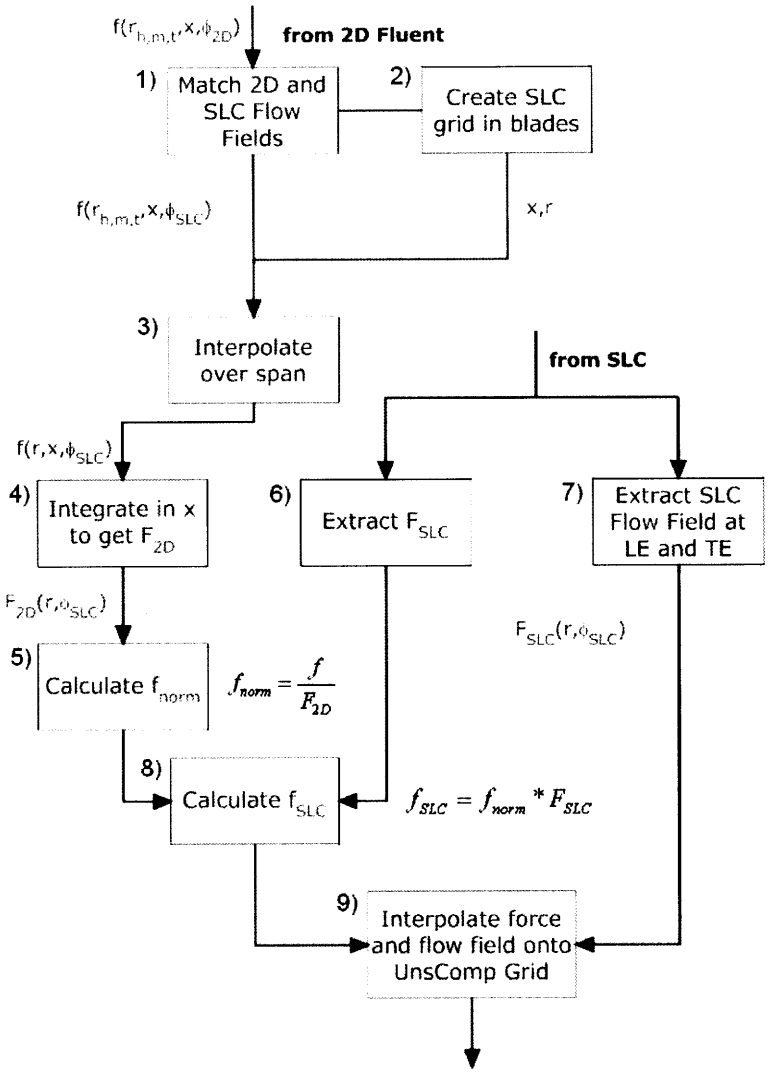

Figure 4-6: An outline of the body force distribution procedure.

At the top of Figure 4-6, the 2D body force is $f(r_{h,m,t},x,\phi_{2D})$. The incidence calculated in the 2D calculation is matched to the incidence from SLC. The forces are smoothed at the leading edge and sampled to the same percentage of the chord at the three radial locations.

This results in $f(r_{h,m,t},x,\phi_{SLC})$.

The grid within the blade row is developed assuming straight streamlines (in the xr plane) that connect the leading and trailing edges. In step 3 in Figure 4-6, the x,r grid is used when interpolating $f(r_{h,m,t},x,\phi_{SLC})$ over the span to give $f(r,x,\phi_{SLC})$. This interpolation assumes the form of the distribution varies linearly from hub to tip. Along each streamlines, the distributed force is integrated and distributions normalized by their magnitude, F_{2D} resulting in f_{norm} (Eqn. 4.1).

$$f_{norm} = \frac{f}{F_{2D}} \tag{4.1}$$

To scale the distributions (step 8 in Figure 4-6), f_{norm} is multiplied by F_{SLC}, the total blade force extracted from the SLC flow field (Eqn. 4.2). This force as well as the corresponding SLC flow field is interpolated on the UnsComp grid linking ϕ_{local} as required.

$$f_{SLC} = f_{norm} * F_{SLC} \tag{4.2}$$

4.3 Developing the 3D/SLC Body Force

As discussed in Section 2.3 and detailed above, the 2D/SLC body force database can be used in UnsComp. However, we want to use the body forces from three-dimensional calculations when available. This section details the process to develop the 3D/SLC body force database.

4.3.1 Procedure for Joining 3D and SLC

This procedure is based on work by Kiwada (8) and is outlined in Figure 4-7. The body force is extracted from a 3D Navier-Stokes solver for all flow coefficients where solutions are available. In practice, this will likely be from design to the stall point. The forces can come from any 3D solver, but henceforth these body forces will be referred to as "T-block forces", where T-block is the 3D unsteady Navier-Stoker computation used for this project.

Given these T-block forces as well as $\phi_{overall}$, the point where the SLC forces are joined is determined. This point, ϕ_{slocal_A}, is set to be 5% lower than the last T-block local flow coefficient to facilitate a smooth attachment. In step 3 the SLC force for attachment, F_{SLC_A}, is determined from the total body force extracted from SLC, F_{SLC}. The F_{SLC_A} include the

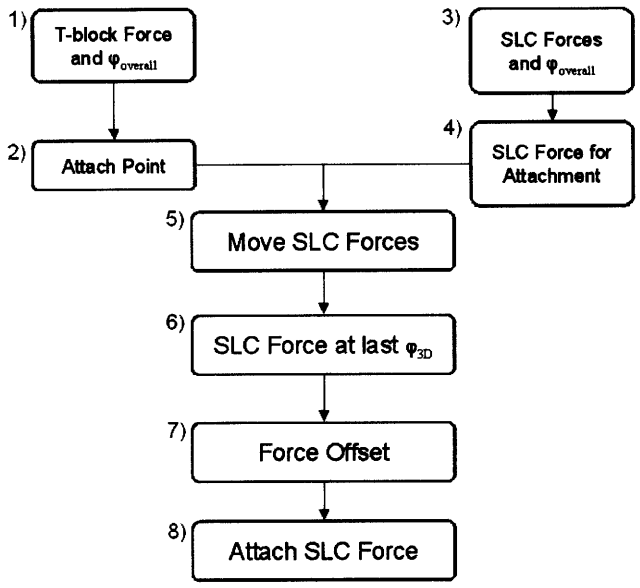

Figure 4-7: Flow chart detailing the body force attach procedure.

SLC peak if a peak is not computed in T-block. If a peak is computed in T-block, the force .1Φ past the SLC peak and below is used since the slope of the body force curve is already positive. This is to avoid having two peaks.

The F_{SLC_A} are translated to ϕ_{slocal_A} in step 5. This causes the 3D and SLC forces to overlap since the F_{SLC} at greater than ϕ_{slocal_A} have to be removed. In step 6 the value of F_{SLC} is calculated at the last ϕ_{3D} by linear interpolation using the two ϕ_{SLC} that bracket the last ϕ_{3D}. By definition, one of these bracketing values of ϕ is ϕ_{slocal_A} and the other the first overlapping ϕ. Once the value of F_{SLC} is determined, the difference between F_{3D}, the total body force from T-block, and F_{SLC} is calculated at ϕ_{3D} to determine their offset. The F_{SLC_A} are then translated this amount to match the last F_{3D} and overlapping F_{SLC} points are discarded.

4.3.2 3D/SLC Body Force Results

The above process is designed to give a smooth body force database. In Figure 4-8, the rotor and stator meanline forces are shown. Notice that the peak of the axial force on the stator was computed using T-block forces so only the positively-sloped portion of the SLC forces are attached.

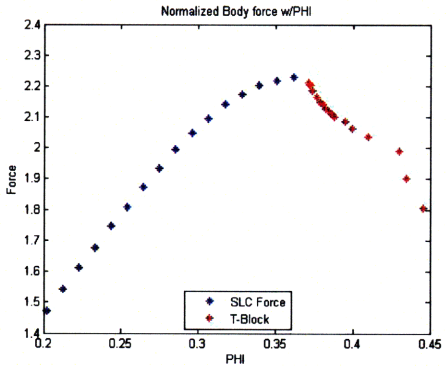

(a) Rotor Meanline 3D/SLC Force

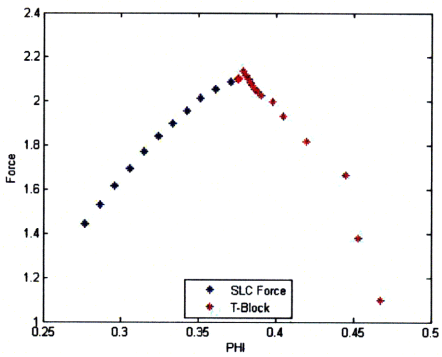

(b) Stator Meanline 3D/SLC Force

Figure 4-8: Assembled 3D/SLC force at the meanline for the rotor and the stator. The transition in both cases is smooth.

Near the rotor tip (say from 70% to 80% span) making a smooth connection is more difficult. Figure 4-9(a) shows the slope of curve of the T-block force is nearly zero and the slope of the curve the force from SLC is positive. Given the current procedure, discontinuities in the slope of the attached force are difficult to avoid due to differences in the local flow field in the T-block calculation and SLC calculations.

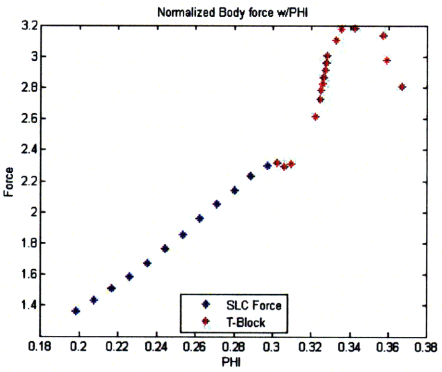

(a) Rotor Near Tip 3D/SLC Force

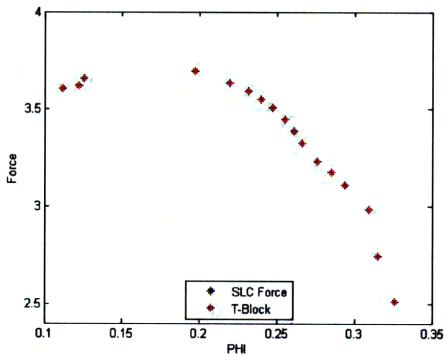

(b) Rotor Tip 3D/SLC Force

Figure 4-9: Assembled 3D/SLC force at the near the rotor tip and at the rotor tip. "Near the rotor tip" refers to one cell away from the tip.

To mitigate this problem we use F_{3D} whenever possible. In Figure 4-9(b), the force in the tip cell (96-100% span) of the rotor is shown. For that span, the local flow coefficient is low enough so that the 2D/SLC body forces are not needed.

This procedure results in $f(x, r, \phi_{overall})$, a combination of T-block and SLC forces.

These forces are linked, using both the T-block and SLC flow fields, to ϕ_{local} to create the 3D/SLC body force database.

4.3.3 Assembly Shortcomings

This combination of force gives a more accurate description of the body before the stall point than streamline curvature only, however, the advantage in using the 2D/SLC body force database is the smooth transition between the unstalled and stalled body forces. Even in a situation like that in Figure 4-8, where the force connection is smooth, there can be a discontinuity at the attachment point due to the difference in the chordwise distributions. Figure 4-10 shows the normalized force and local phi in one cell illustrating the discontinuity. At this point, it is not clear how this discontinuity affects stability estimation. Chapter 6 will addresses this issue.

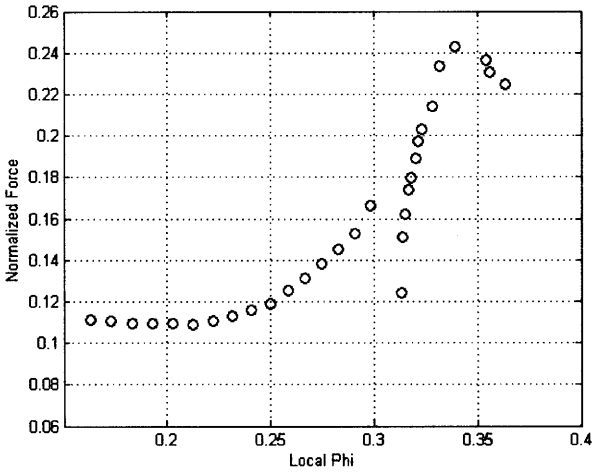

Figure 4-10: Example of local discontinuity in the body force database. The plots shows the local force vs. local phi at one cell in the domain, specifically on the rotor at 50% chord and 70% span.

Chapter 5

Assessment of the Stall Prediction Methodology

This chapter discusses the assessment of the stall prediction methodology using the 2D/SLC body force database. The goals of this assessment along with the procedure and results are discussed.

5.1 Assessment Goals

Although each part of the 2D/SLC model has been separately assessed (Appendix C), we need to check the stall prediction methodology end-to-end. One focus of the assessment is the axisymmetric flow field computed by UnsComp compared to the flow field calculated by SLC. Since the body force for the streamline curvature is input into UnsComp, a consistent flow field would also mean that the models and approximations built into the methodology were consistent and would also check the axisymmetric UnsComp. (Although UnsComp was shown to work by Gong (4), the code has been modified for use in this project and thus is still in need of assessment.)

The reason for assessing the axisymmetric flow field is that an axisymmetric calculation needs to be completed before any unsteady calculations. The characteristics calculated in SLC and UnsComp and the radial profiles of ϕ and ψ should be basically the same since the body force from SLC is used as the input to UnsComp. There will be some differences, however, since the streamline curvature does no handle reversed flow. (The SIMSLEQ code has a limiter preventing flow reversal.)

5.2 Assessment Procedure

The parts of the stall prediction methodology to be assessed are marked with numbers on Figure 5-1, an overview of the assessment methodology using the 2D/SLC model. The first step, a portion of the 2D/SLC model, confirms that the body force was generated correctly. It is shown that f_{SLC} (see Figure 4-6) does integrate to F_{SLC}, confirming that the 2D distribution was correctly scaled to the SLC total body force. Also, it is shown that the flow field and force are the same after they are interpolated from the SLC grid onto the UnsComp grid. The methodology features contributions from many codes associated with separate effects, making it essential to be sure that the output from one code is the input to the next(box 2).

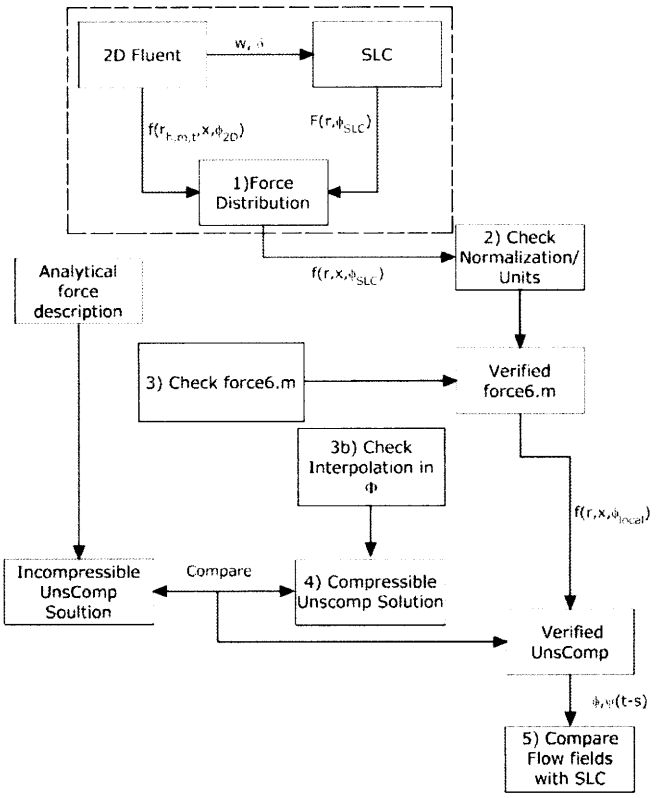

Figure 5-1: Flow chart detailing the stall prediction methodology assessment. The dashed-box which encloses the top three boxes is the 2D/SLC model.

The code that links the flow field, $\phi_{overall}$ to ϕ_{local}, referred to as force6, is part of the preprocessor for UnsComp and needs to be verified. Box 3 is ensuring that the input into

force6 is the same as its output.

Box 3b) is assessing UnsComp's interpolation procedure. UnsComp operates by using the local flow coefficient to interpolate to the body force database which is used to update the flow field. The assessment is to confirm that UnsComp is handling the input database correctly.

In previous work, Gong(4) developed an analytical procedure based on the experimental characteristics to obtain the body forces. These body forces were input into an incompressible version of UnsComp and the result used for the assessment of the compressible version of UnsComp.

The 2D/SLC body force database was input into the validated force6 and a validated UnsComp and the results of the calculation compared to the flow field and characteristics processed from the SLC solution. The five step procedure the completely assesses the stall prediction methodology.

In summary, the first two steps made sure the force from 2D/SLC is correct and compatible with force6. The body force inputs into UnsComp were checked. The UnsComp internal routines and compressible version are checked. The flow field is also checked against known results.

This procedure was developed for use with the 2D/SLC body force database. If T-block were to be used for extracting unstalled body forces the assessment would be the same with the addition of a verification to check that the forces were joined properly. As of this point, the 3D/SLC body force database has not been used in UnsComp and the procedure is not fully developed.

5.3 Assessment Results

5.3.1 Body Force Input

The body force input to UnsComp was integrated along the chord and compared to the total body force extracted from SLC. The force was interpolated from the SLC grid to the UnsComp grid, integrated along the chord, and plotted on the same plot. Figure 5-2 shows the axial force near design, $\Phi = .976$. There are slight differences between the SLC force and UnsComp and the integrated 2D/SLC force is matched exactly.

Shown in Figure 5-3, near the stall point there is an 8% difference in the axial force on

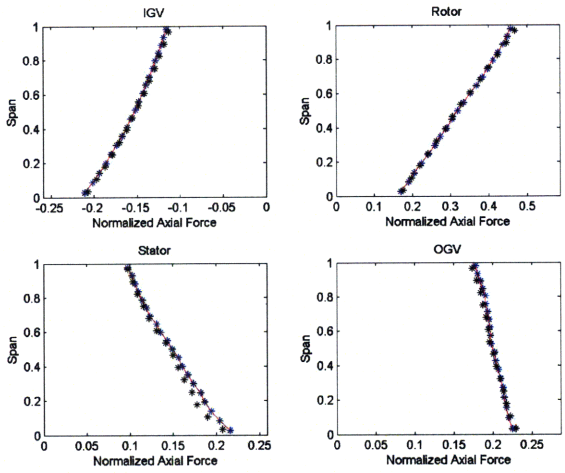

Figure 5-2: Integrated 2D/SLC axial force (blue), SLC axial force (red line), axial force on the UnsComp grid (black) versus span for each blade row for $\Phi = .976$.

the OGV near the hub and tip. The rotor and stator match up well. In all cases the total force from SLC matches the integrated 2D/SLC force to within .5%. It's not shown but the tangential force is also matched well.

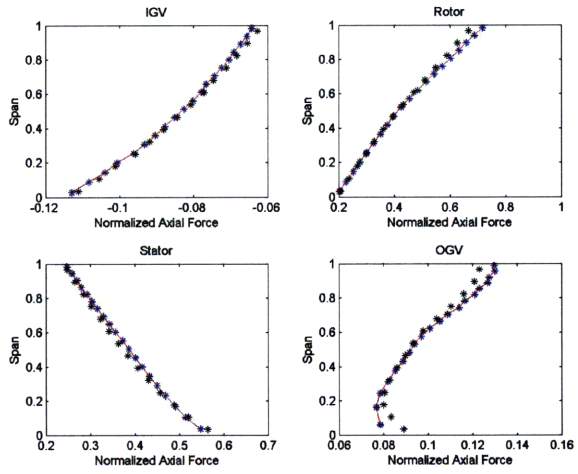

Figure 5-3: Figure compares the integrated 2D/SLC axial force (blue), the SLC axial force (red line), and the axial force on the UnsComp grid (black) for each blade row at stall.

The units of the body force are $\frac{[Force]}{[Mass]}$ or acceleration(8).

$$F_x = \frac{[flux]A_{cell}}{br\rho V_{cell}} \left[\frac{m}{s^2}\right] \tag{5.1}$$

The term $flux$ is the total flux leaving the cell, in units of pressure (from solving Eqns. A.4-A.7 for the axial force). UnsComp needs the force in units of $\frac{1}{[length]}$. This is handled in force6 which puts the local force in these units (Eqn. 5.2).

$$F_x = \frac{F}{[Mass]} \frac{1}{U^2_{local}} (4) \tag{5.2}$$

In preparing the body force, force6 interpolates the database onto a given set of local flow coefficient and organizes the data for the input into UnsComp. Figure 5-4 compares the input force into force6 (labeled Kiwada) to the output of force6. If the code is working correctly these plots should match as they do so the correct force is being input into UnsComp.

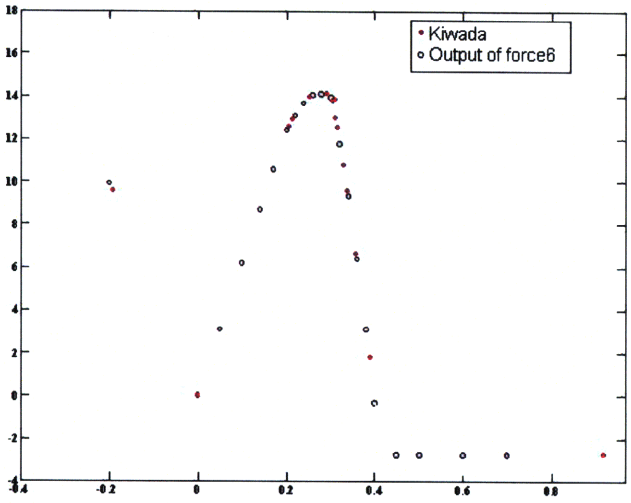

Figure 5-4: Input axial forces (labeled Kiwada) compared to the output axial force of force6 at the rotor leading edge.

5.3.2 UnsComp

Step 3b) assesses the internal interpolation routine in UnsComp. The axial body force output from UnsComp was compared to the input force database (interpolated to the same flow coefficient(11)). These are plotted at the leading and trailing edges of the rotor in

Figure 5-5. The comparison of the unsteady behavior has not been carried out. This The step is bypassed at this time because it looks at the unsteady behavior which is not a priority in this assessment procedure.

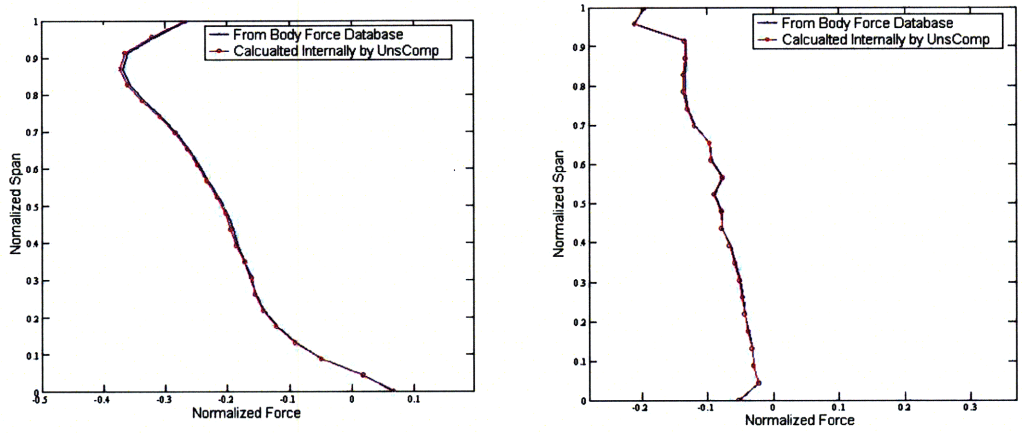

(a) Rotor LE UnsComp Force Comparison

(b) Rotor TE UnsComp Force Comparison

Figure 5-5: Tangential force calculated internally in UnsComp compared to the body force from the original database(11).

5.3.3 UnsComp Flow Field

An additional check is to confirm that the UnsComp axisymmetric calculation can reproduce the SLC flow field. The characteristic for SLC, the test data, and UnsComp results all shown in Figure 5-6. The UnsComp and SLC characteristics match from design to the stall point. Past the stall point the UnsComp characteristic drops off because reversed flow develops at the blade row tip.

Figures 5-7 and 5-8 show ϕ and ψ profiles near design. Near design the profiles match well, but near stall (Figure 5-9) there are differences, especially on the rotor, where there is a 6% (max) difference in the pressure rise.

This assessment procedure shows the body force description and the axisymmetric methodology are self-consistent. The next step is to determine if the compressor modeled using the 2D/SLC body force database shows the same unsteady behavior seen in the test data.

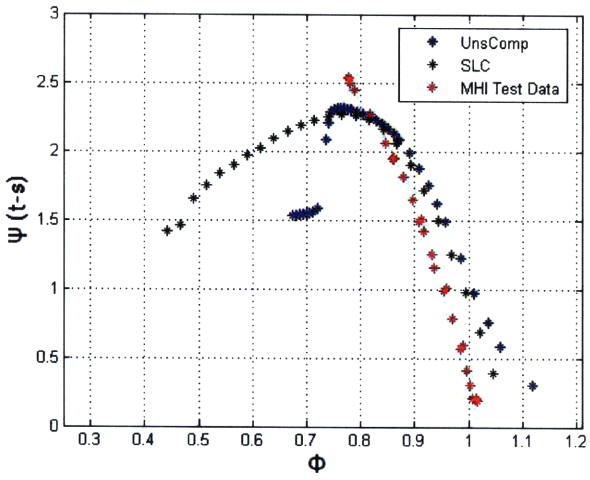

Figure 5-6: Comparison of the UnsComp, SLC, and test data characteristics. Note that the UnsComp characteristic $\psi(t-s)$curve begins to drop sharply at the peak.

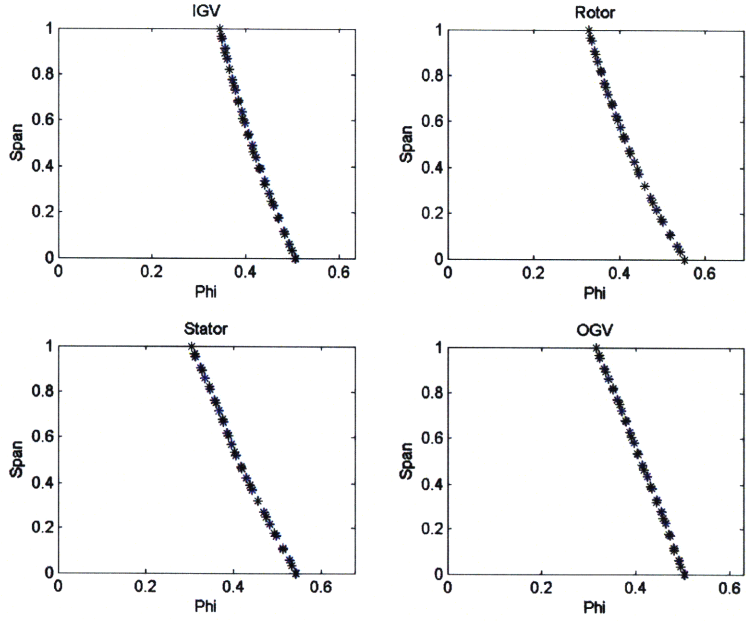

Figure 5-7: Comparison of UnsComp and SLC phi profiles at design.

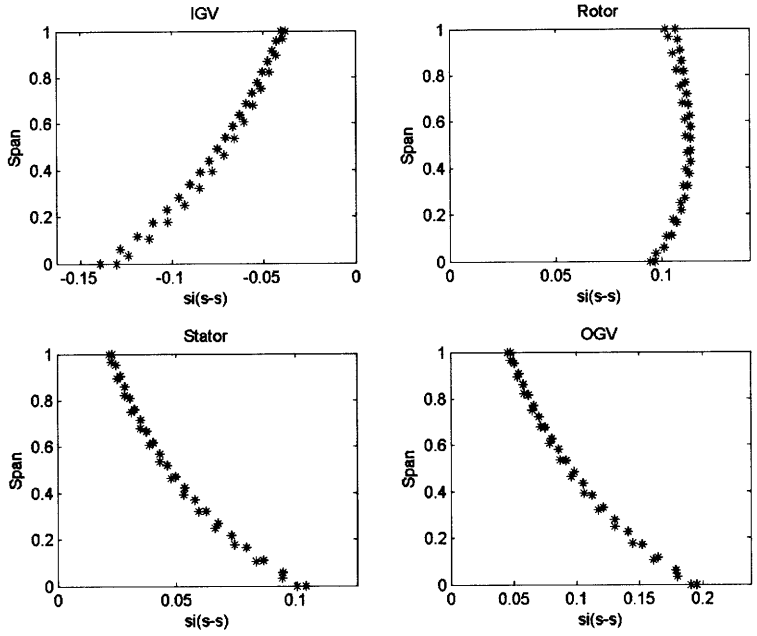

Figure 5-8: Comparison of UnsComp and SLC si(s-s) profiles at design.

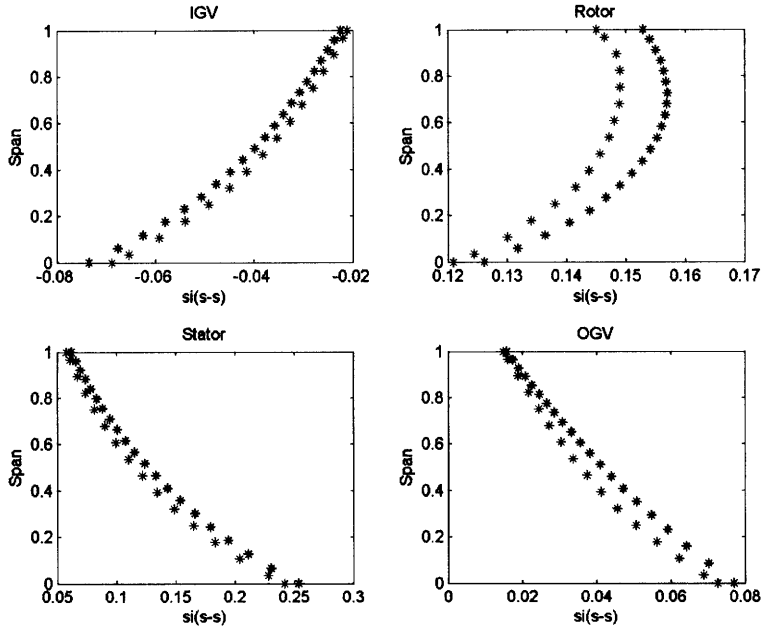

Figure 5-9: Comparison of UnsComp and SLC si(s-s) profiles at stall.

Chapter 6

Sensitivity of the Stability Estimation to Stalled Body Forces

This chapter discusses the unsteady behavior of the compressor as described by the 2D/SLC body force database. The unsteady, compressible version of UnsComp is used. These results are the baseline in the sensitive study which determines the importance of the body force distribution to stall onset.

6.1 Stability Analysis

The goal of the stability analysis is to determine the stall point. The type of stall inception (modal or spike) is also important. The final form of instability, full or part span rotating stall, ring stall, or surge, is of less importance. The single stage compressor was described using the 2D/SLC body force database because the unsteady 3D calculations using T-block have yet to be completed. The plan is to use the 3D/SLC body force database when the T-block solutions become available.

The unsteady calculation is run by perturbing an axisymmetric solution with a disturbance. If the input disturbance decays and the solution returns to a steady state then the flow is stable. If the disturbance grows the flow is unstable.

In the actual environment, disturbances may arise from any number of flow events or environmental features present. The input disturbance was that used by Gong(4), which has a large amplitude and thus contains a wide spectrum of frequencies. Gong showed that using the same input either inception type can develop and lead to stall (4) as seen in Figure

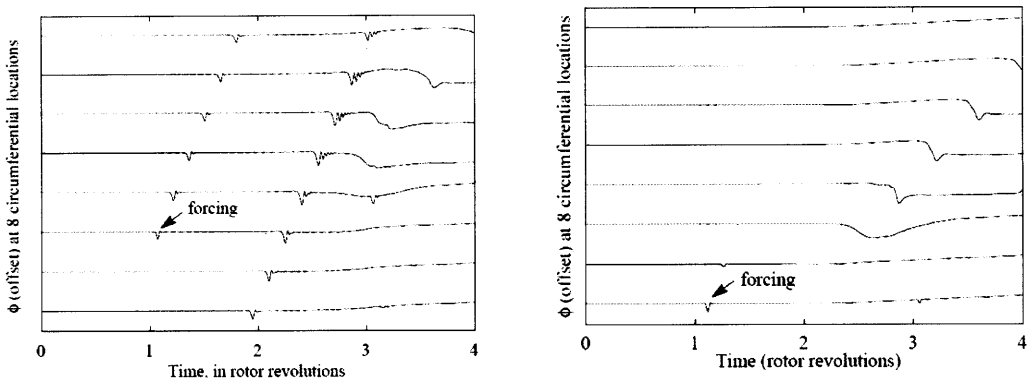

(a) Stall through short wavelength disturbances (spikes)

(b) Stall through long wavelength disturbances (modes)

Figure 6-1: Illustration of stall through spike and modes for the same forcing input(4).

6-1(a). Traces of the flow coefficient at different circumferential stations around the annulus which shows, in Figure 6-1(a), the disturbance immediately begins to grow developing into the beginnings of a stall cell by the third rotor revolution. In contrast, in Figure 6-1(b), a small amplitude mode develops before stall.

The characteristics of the input disturbance can be changed depending on goals of the analysis. The parameters are forcing blade row (rotor or stator), location of the forcing (hub, mean, or tip), length of time between inputs, forcing duration, width, forcing magnitude, and interval. For this thesis calculation, the blade row and the spanwise location are at the rotor tip region because this is where the spike initiates in the experiment. Table 6.1 gives the inputs.

The input tables represent two cases one with the forcing magnitude decreased by a factor of one hundred. The large input causes a loss of 50% of the local pressure rise. The acceptable range of 20% to 60% was determined by Gong(4). The small amplitude input only causes a loss of 1% of pressure of local pressure rise. This input was only used in cases where the type of stall inception was unclear from the ϕ traces. The forcing interval was set to forty rotor revolutions and in most cases, the flow was only computed for 10-20 revolutions because by then the flow had either stalled or stabilized. The other two parameters duration and width were set at values determined by Gong(5).

Parameter	Value
Blade Row	Rotor
Spanwise Location	Tip
Start time	$\frac{1}{2}$ revolution
Interval	40 revolutions
Magnitude	15
Duration	$\frac{1}{10}$ revolution
Width	2 blade pitches

Parameter	Value
Blade Row	Rotor
Spanwise Location	Tip
Start time	$\frac{1}{2}$ revolution
Interval	40 revolutions
Magnitude	.15
Duration	$\frac{1}{10}$ revolution
Width	2 blade pitches

Table 6.1: Input forcing disturbance parameters for spike input(left) and for modal input(right). In the table on the right, the forcing magnitude is reduced by a factor of a hundred.

6.2 Baseline Calculations

Calculations were run on the negative side of the characteristic (Figure 5-6) starting at $\Phi = .82$, with the flow rate reduced until stall occured. The type of stall inception was determined by examining the ϕ traces.

6.2.1 Calculations with the OGV

The first calculations used a geometry consisting of the IGV, rotor, stator, and OGV. For conditions where the rotor was stable (input disturbance dies away) a modal pattern consisting of eight lobes arose in the OGV. These modes were also seen in the stator and in the rotor with decreased amplitude. Traces of the mode are shown in Figure 6-2, and a snapshot of the ϕ shown in Figure 6-3. The disturbance rotates at about 20% of rotor revolution speed, a behavior seen for modal disturbances(1).

Figure 6-4 shows traces at the rotor leading edge where no disturbance is seen. (The rotor is by itself stable at this condition.) As the flow rate is reduced, the amplitude of the OGV disturbance grows. At the stall point, the modes' presence make the stall inception type difficult to interpret.

Traces show that the mode is associated with the OGV, and thus is consistent with the blade row characteristics. At the design point, $\Phi = 1$, the slope of the OGV characteristic is positive while both the rotor and stator have negative slopes (Figure 6-5).

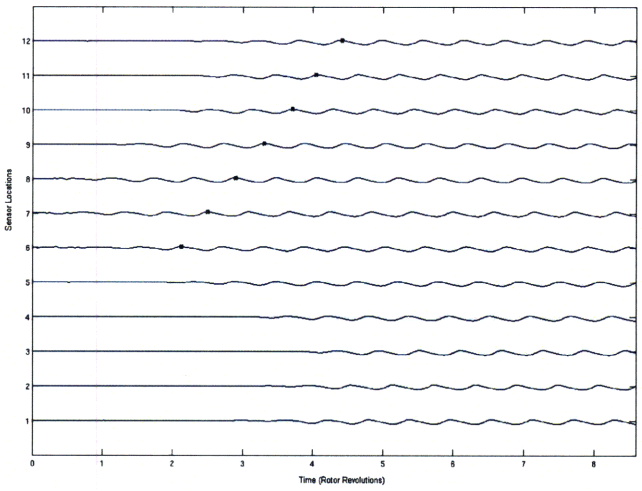

Figure 6-2: ϕ traces at twelve equally spaced circumferential locations (30° apart) at the OGV trailing edge at $\Phi = 1$. One lobe of the modal pattern is tracked as it rotates.

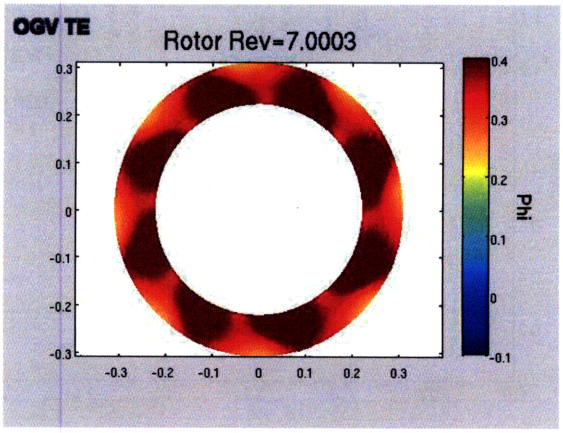

Figure 6-3: Snapshot of the ϕ at the OGV trailing edge around the annulus depicting the modal pattern in the OGV at $\Phi = 1$.

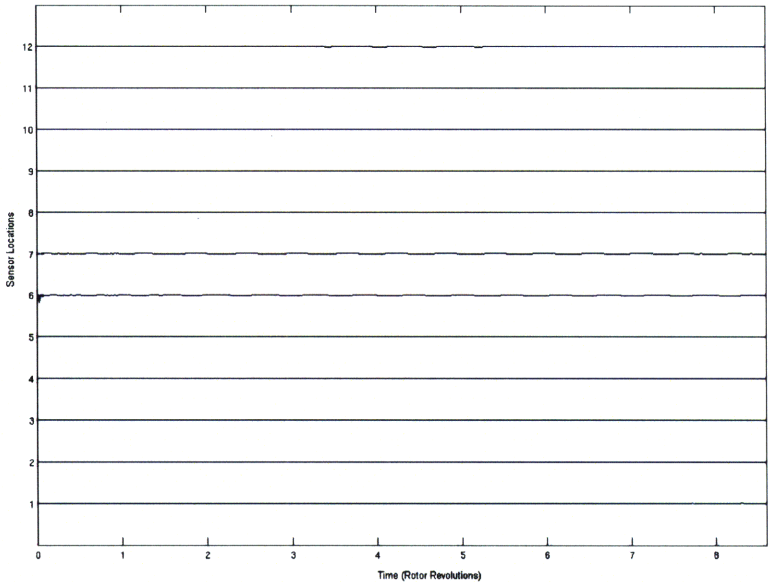

Figure 6-4: ϕ traces at twelve equally spaced circumferential locations (30° apart) at the rotor leading edge at $\Phi = 1$. Disturbance is nearly non-existent.

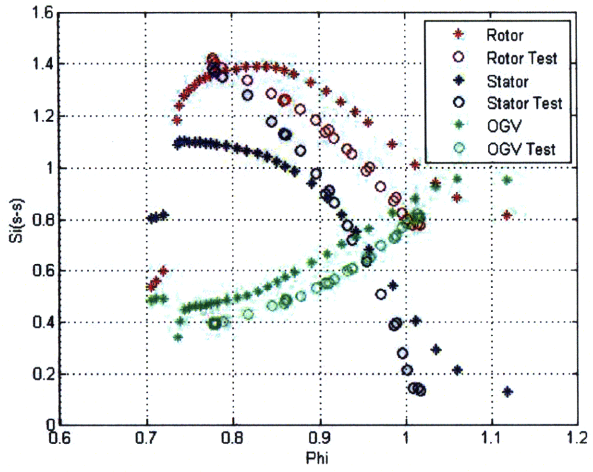

Figure 6-5: Blade (s-s) characteristics for UnsComp and the test data. The slope of the rotor(red) and stator(blue) curves are negative at $\phi = .41$ ($\Phi = 1$) and the OGV curve positive.

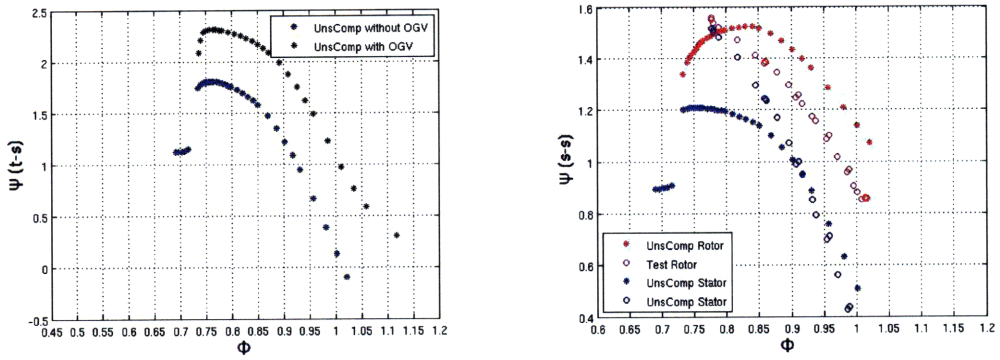

(a) Comparison of the overall characteristic with and without the OGV

(b) Rotor and Stator blade characteristics without OGV compared to the test data

Figure 6-6: New characteristics with the OGV.

6.2.2 Calculations without the OGV

To confirm the role played by the OGV, calculations were run setting the body force on the OGV to zero thus removing the blade row from the calculation. The overall and blade row characteristics for this calculation is shown in Figure 6-6. The pressure rise is reduced by 20% compared to the computations with the OGV. Unsteady calculations without the OGV, at flow coefficients where the rotor is stable, show no modes in the IGV, rotor, stator, or downstream. Traces at the stator trailing edge with the OGV and without the OGV are compared in Figure 6-7. The conclusion is that the OGV stall causes the modal pattern at high flow. The behavior of the OGV is of little importance to this project and since the rotor and stator, as well as the general shape of the overall characteristic, are not affected, all calculations were run with the OGV body force set to zero.

The first flow coefficient where the input disturbance was sustained was $\Phi = .777$. $\Phi = .78$ is the condition where stall develops in the experiments. The final form of the instability was one part-span rotating stall cell (Figure 6-10(a)). The experimental data is inconclusive in whether the final form was full or part span rotating stall but the experiments showed spike stall.

The development from the input spike disturbance to the stall cell in the computation does not exhibit behavior clearly characteristic of spike stall inception. The ϕ traces are shown in Figure 6-8. The figure shows that the input spike maintains its magnitude from one half to approximately six revolutions before decaying. A eight lobe modal pattern then

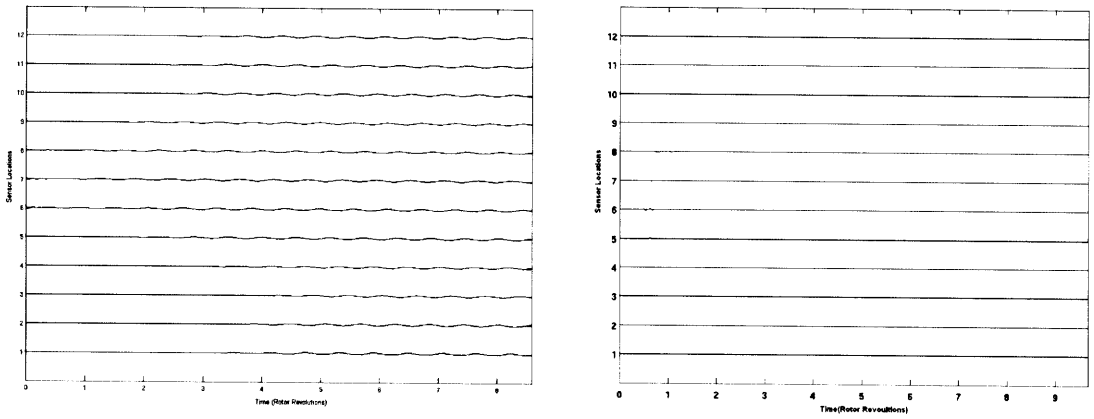

(a) With OGV

(b) Without OGV

Figure 6-7: ϕ traces at twelve equally spaced circumferential locations (30° apart) at the stator trailing edge at $\Phi = 1$ for computation with and without the OGV.

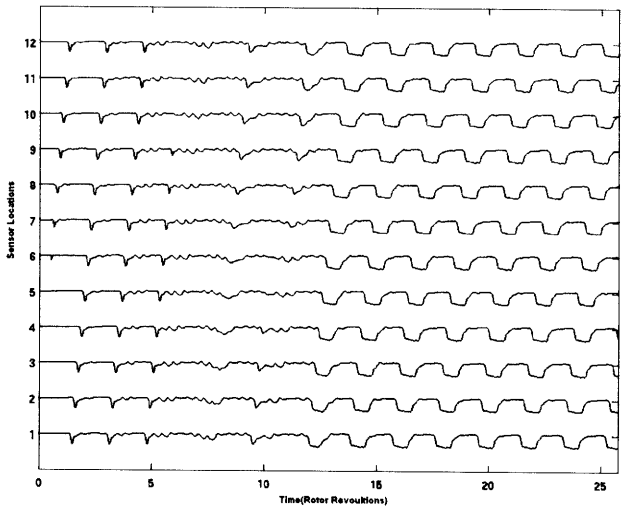

Figure 6-8: ϕ traces at twelve equally spaced circumferential locations (30° apart) at the rotor trailing edge at $\phi = .3184$. Large amplitude disturbance is input. Rotating stall begins at about 12 rotor revolutions.

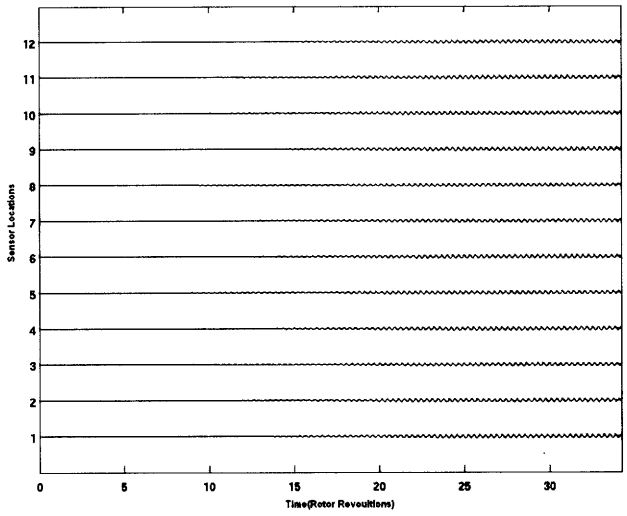

Figure 6-9: ϕ traces at twelve equally spaced circumferential locations (30° apart) at the rotor trailing edge at $\phi = .318$. Small amplitude disturbance is input. Limit cycle starts at about 25 rotor revolutions.

begins propagating before part-span rotating stall develops at the twelfth revolution, leaving the possibility the machine is modal. The blade characteristics near the peak (Figure 6-6(b)), at $\Phi = .777$ the rotor has already stalled and has a positive-slope. To determine whether the compressor is modal the computation was run this same Φ using a disturbance with amplitude reduced by a factor of a hundred (Figure 6-9). The result was eight lobe pattern which develops into a small amplitude, 25% of mean flow, limit cycle, captured in a snapshot shown in Figure 6-10(b). The amplitude of the disturbance as a function of time at the rotor and stator trailing edge is shown in Figure 6-11.

The results is that at $\phi = .777$ there are two possible forms of instability dependent on the input disturbance, but the only disturbance that leads to rotating stall is the spike type. The development from that disturbance to the rotating stall cell is different than observed in the test. The reason proposed is the difference in slope of the characteristics at the stall point. Despite the differences, the conclusion from the stability analysis using the 2D/SLC body force database is that a spike is required for the single stage compressor to go into rotating stall.

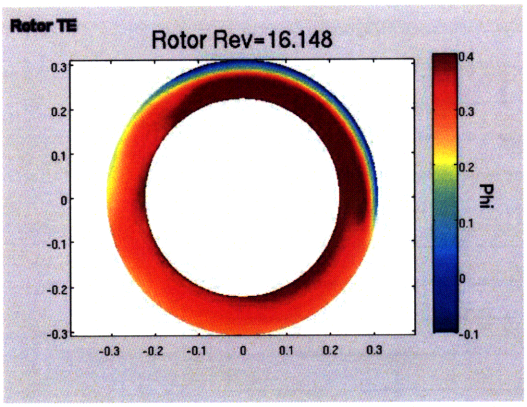

(a) Final form is part span rotating stall for spike input

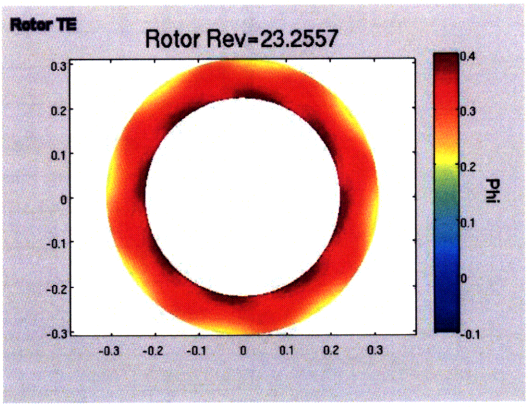

(b) Final form is part span rotating stall for modal input

Figure 6-10: Snapshots of the flow field at the rotor trailing edge for the spike and modal inputs.

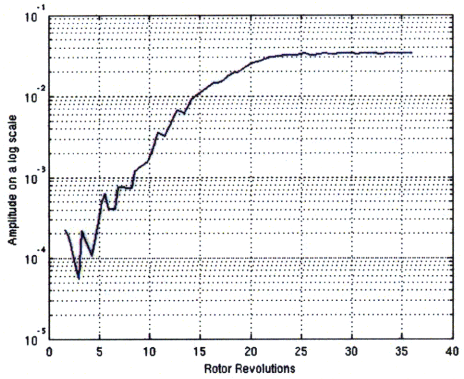

(a) Amplitude of the Disturbance at the rotor trailing edge

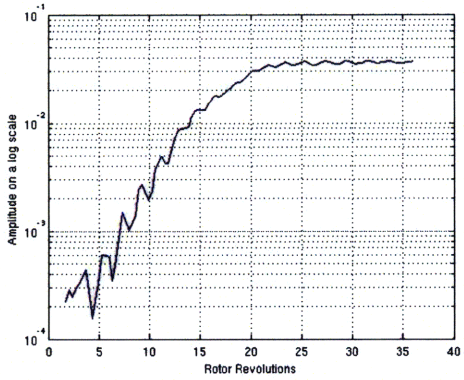

(b) Amplitude of the Disturbance at the stator trailing edge

Figure 6-11: Amplitude of the disturbance at the rotor and stator trailing edge. Note the similarity of the amplitude between the blade rows once it enters the limit cycle. This is due to little damping in the stator at this ϕ.

6.3 Sensitivity Assessment

It is important to understand the link between body force distribution, stall point, and stall inception type. In this, the focus is on the rotor body force at flow coefficients below the stall point since the unstalled forces will ultimately come from T-block and rotor is the blade where the disturbance augments. The parameters are F_x, F_θ, and $f(x)$, the chordwise distribution of force along each streamline, for $\Phi_{overall} \leq .780$, the measured experimental stall point. We wish to determine (1) the sensitivity of the stall point, Φ_{stall}, to changes in the above parameters, and (2) the parameters that are most important in determining the unsteady behavior at stall. In addition, we seeks to explain the unsteady behavior in terms of features of the axisymmetric characteristic and flow profiles.

We will examine the influence of three features of the body force past the stall point: the radial distribution, the axial (chordwise) distribution, and the functional dependence on $\Phi_{overall}$. Determining the effects of the axial and radial distributions allows for assessment of the forces derived from the 2D/SLC model and provides the framework for the development of a set of guidelines for future body force descriptions. This thesis only addresses the first two points in detail. For the functional dependence on $\Phi_{overall}$, some discussion is given of work by Gong(5).

6.3.1 Radial Distribution

Six cases were considered as part of the assessment of the radial distribution of force. For each case the difference in force from the baseline varied linearly with distance from the mean radius. The maximum change in force, at either the hub or tip, is shown in Table 6.2. For all cases, the overall force on the blade was held fixed. For example, in case 1 the axial force was reduced by 30% and the axial force at the hub was increased. The tangential force was held constant. In Figure 6-12, the axial force used in case 1, 2, and 5 is shown.

The change of 30% in cases 1 and 3 was chosen to resemble the tip body force extracted from T-block. In case 2, the axial force was reduced by one quarter of the amount in case 1 to determine sensitivity. Cases 4-6 represent forces that might be seen in a machine that has rotor hub separation in the rotor. Those cases also assess how sensitive a tip critical machine is to changes at the hub.

Case Number	Description
Case 1	30% reduction of F_x at Rotor Tip
Case 2	7.5% reduction of F_x at Rotor Tip
Case 3	30% reduction of F_t at Rotor Tip
Case 4	15% reduction of F_x at Rotor Hub
Case 5	7.5% reduction of F_x at Rotor Hub
Case 6	7.5% reduction of F_t at Rotor Hub

Table 6.2: List of cases for the radial distribution part of the sensitivity assessment.

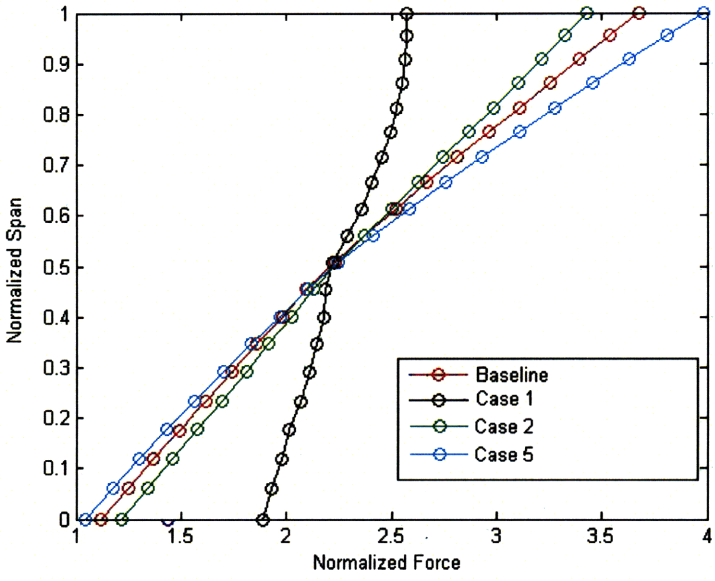

Figure 6-12: The distribution used for baseline and case 1, 2, 5.

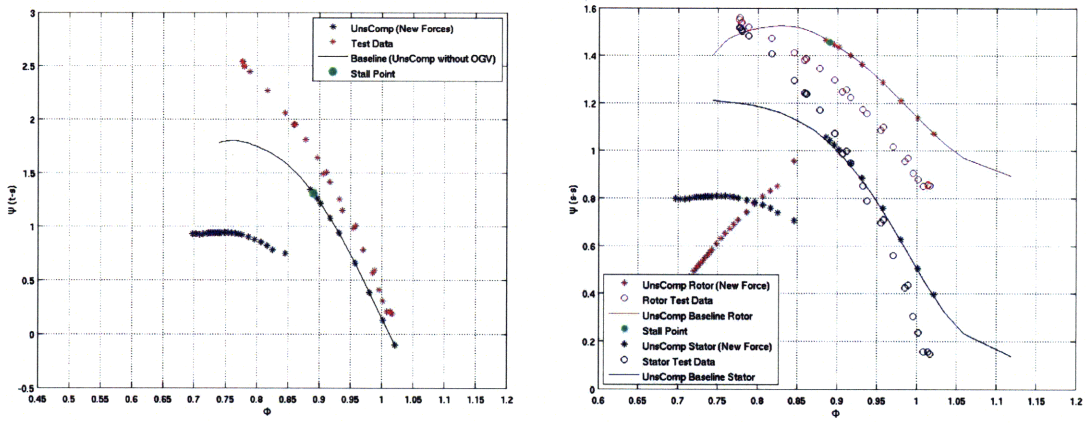

(a) Overall characteristics

(b) Blade characteristics

Figure 6-13: Comparison of characteristics for case 1 to baseline case and test data. The computed stall point is marked in green. Note sharp drop in pressure rise at $\Phi = .875$.

6.3.1.1 Reduced Tip Force

The characteristics for case 1 are shown in Figure 6-13. Reducing the axial force at the tip of the rotor results in a change in stall point and in spike stall inception. There is also a ring stall exhibited at a higher flow coefficient ($\Phi = .87$). The characteristic from the baseline cases (Figure 6-6(b)) show a smooth transition between unstalled and stalled flow, however, case 1 exhibits a sudden drop in pressure rise at $\Phi = .87$ because of the development of ring stall. The spikes, seen in Figure 6-14, develop into a part-span rotating stall cell at $\Phi = .89$, a 15% larger flow coefficient than the baseline case.

Case 2 shows that behavior to a lesser degree. The characteristics are shown in Figure 6-15. There is a small change in axial force at the tip and a smaller differences in the characteristics from the baseline. The development of ring stall occurs at a lower flow coefficient than in case 1. The stall point is on the positive side of the characteristic, located at $\Phi = .792$ (2% larger than the baseline case), but the stall inception type is still spike (Figure 6-16). Looking at Figure 6-15(b), it is possible that the stator is stabilizing the machine since the slope of that characteristic is slightly negative at the stall point.

In case 3, the tangential force was reduced with little change in the axisymmetric characteristics (Figure 6-17). The maximum difference between the overall characteristics is 2%. An order of magnitude less than case 2. The stall point for case 3 is $\Phi = .775$, a half of a percent different from the baseline case and the stall inception type is the same as well,

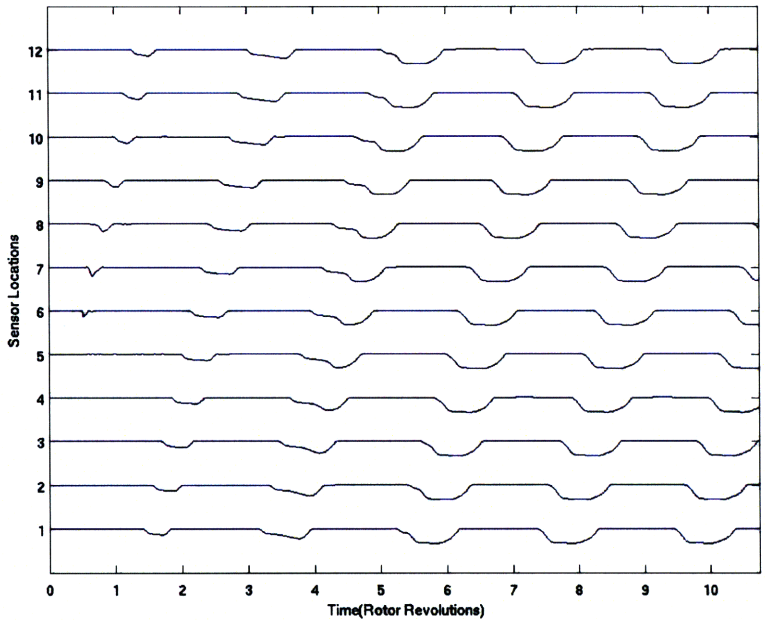

Figure 6-14: ϕ traces at the rotor tip at $\Phi = .89$ with spike inception.

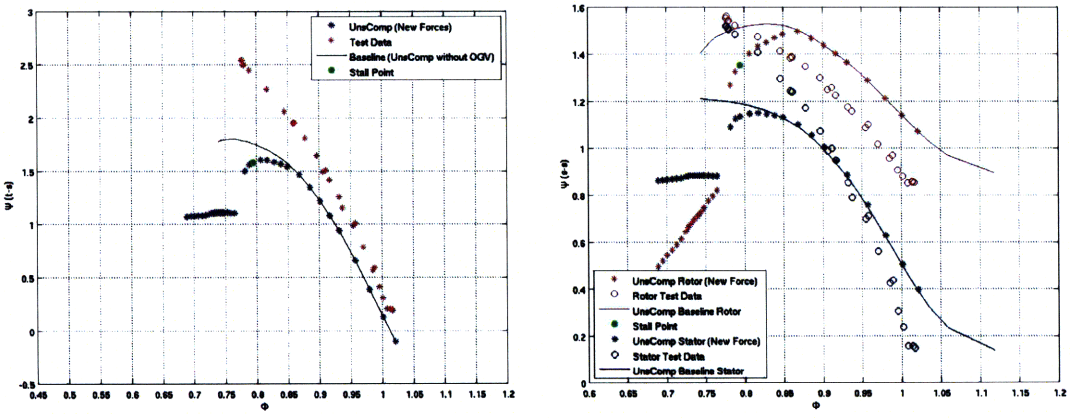

(a) Overall characteristics

(b) Blade characteristics

Figure 6-15: Comparison of characteristics for case 2 to baseline case and test data. The computed stall point is marked in green. Note that the stall point is after the peak.

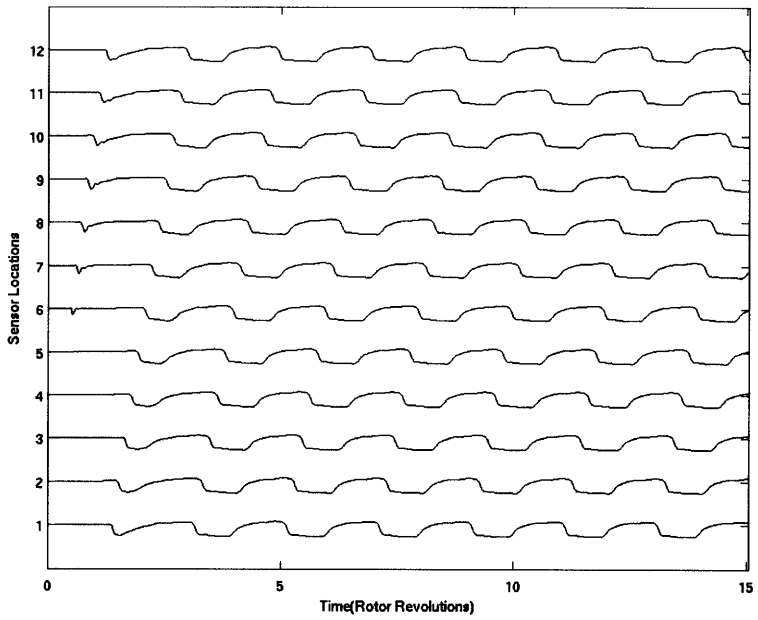

Figure 6-16: ϕ traces at the rotor tip at $\Phi = .792$ with spike inception.

spike. Figure 6-18(b) shows similar behavior as Figure 6-8 and Figure 6-18(a) shows a limit cycle similar to Figure 6-9.

Table 6.3 gives a summary of results for case 1, 2, and 3. The key results are (1) stall inception and the stall point are strongly sensitive to the axial force profile, (2) the solution is much less sensitive to changes in the tangential force, and (3) reducing the axial force at the rotor tip leads to spikes.

Case Number	Φ_{stall}	Inception Type	Final Form
Case 1	$\Phi = .890$	Spike	Part Span
Case 2	$\Phi = .792$	Spike	Part Span
Case 3	$\Phi = .775$	Spike (baseline)	Part Span

Table 6.3: Summary of results at the rotor tip. "(baseline)" refers to spike inception similar to the baseline case.

6.3.1.2 Reduced Hub Force

For case 4 the axial force is reduced by 15% at hub. The characteristics are given in Figure 6-19. The increased force in the tip region suppresses the drop in pressure rise seen in cases 1, 2 (Figure 6-13, 6-19). The stall point (case 4) is located on the positively-sloped

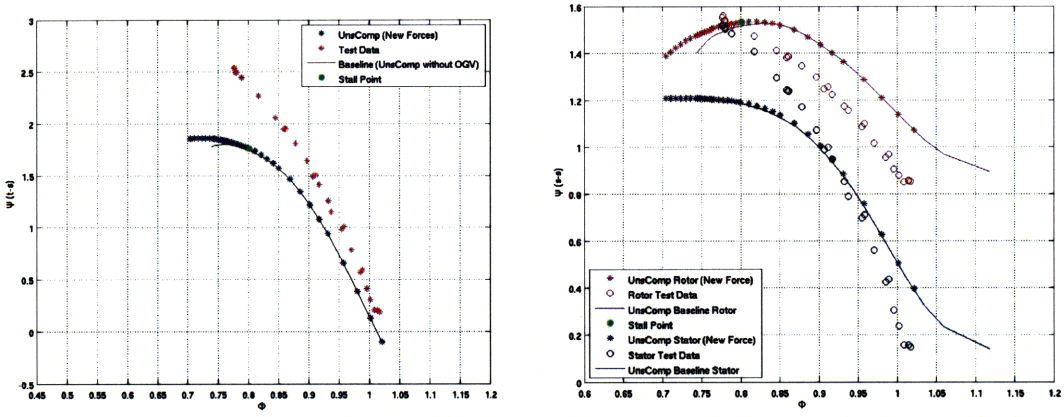

(a) Overall characteristics

(b) Blade characteristics

Figure 6-17: Comparison of characteristics for case 3 to baseline case and test data. The computed stall point is marked in green. The maximum difference between the overall characteristics is 2%.

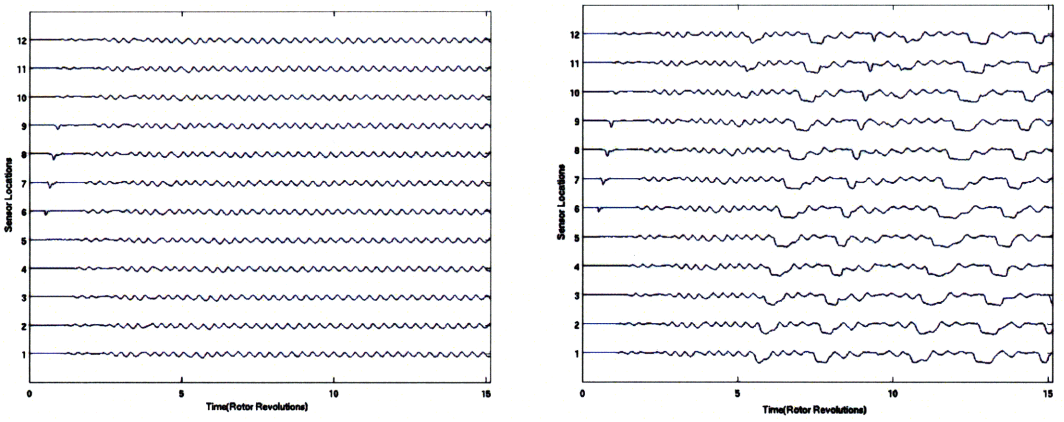

(a) Limit Cycle

(b) Modes and Spikes before stall

Figure 6-18: ϕ traces at the rotor tip $\Phi = .781$ (a) and $\Phi = .775$ (b). The first plot shows a limit cycle developing at 3 rotor revolutions and second plot shows unconventional spike stall.

side of the characteristic at $\Phi = .709$, 9% below the baseline case. Case 1 had a 15% reduction in the stall margin, so the two largest changes in axial force result in the two largest changes in the stall point.

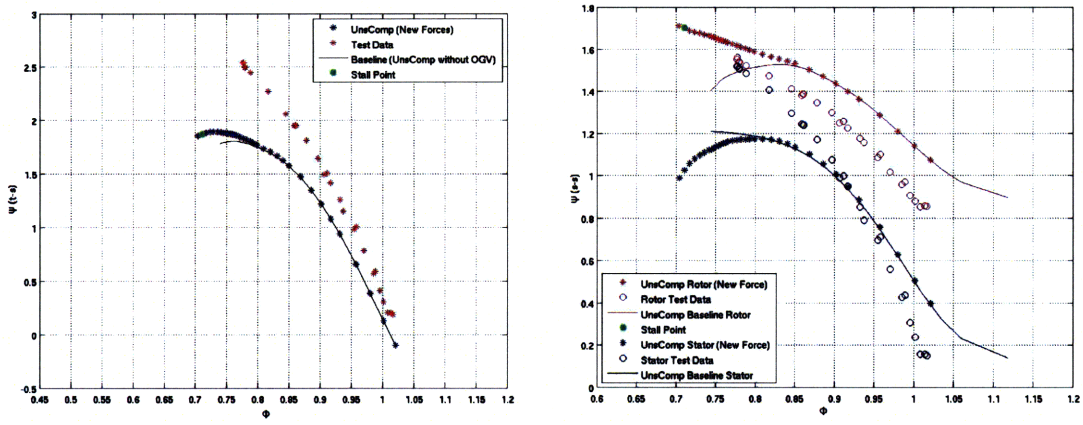

(a) Overall characteristics

(b) Blade characteristics

Figure 6-19: Comparison of characteristics for case 4 to baseline case and test data. The computed stall point is marked in green. Stalls past peak of the characteristic.

The reduction in force at the rotor hub appears to lead to modal stall in that region. Although the spike is input at the tip, the disturbance soon decays (because the tip is healthy) and a stall cell develops at the rotor hub (Figure 6-21(b)). The modes shown in the traces at the hub (Figure 6-20(a)) rotate at 38% of rotor revolution speed. This is behavior, associated with modal stall inception, was identified by Gong(4) and Camp and Day(1).

In the leftmost plot in Figure 6-21(a), the flow in the rotor is seen to be weaker in the hub than the baseline case. The flow in the stator hub is worse than in the rotor (rightmost plot in Figure 6-21(a)), because stator hub tends to separate as Φ_{local} is reduced. The stall cell still appears first in the rotor (Figure 6-20).

Characteristics for case 5 are shown in Figure 6-22. Comparing the characteristic in Figure 6-22 with that in Figure 6-15 (case 2), there is a larger change in pressure rise when the force is reduced at the tip than when it is reduced in the hub (12% maximum difference compared to 3% difference).

Case 5 results show that stall inception type is mildly affected by small changes in axial force. There are no modes, however, the input spike takes 6-7 rotor revolutions (Figure

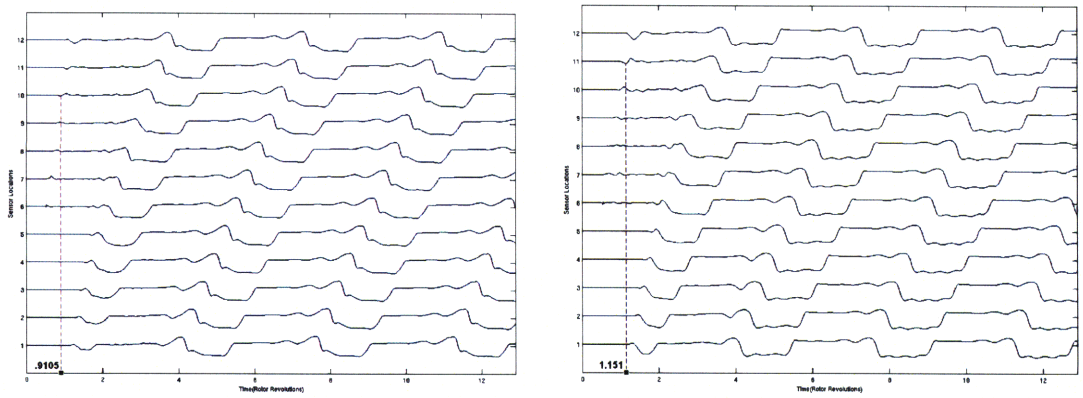

(a) ϕ traces at the rotor hub $\Phi = .709$ (b) ϕ traces at the stator hub $\Phi = .709$

Figure 6-20: Apparent modes develop into a stall cell originating from the rotor hub. The time the modes begin to grow is noted on each plot.

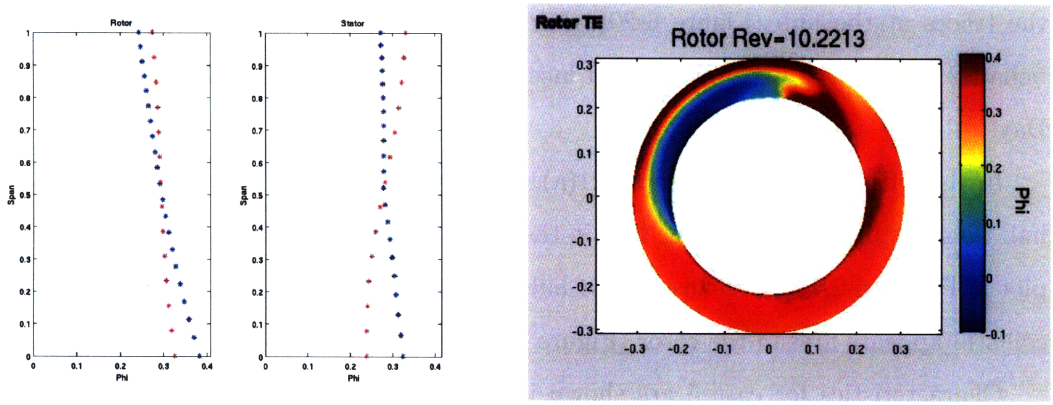

(a) Rotor and Stator ϕ profiles (b) Stall cell at the Rotor Hub

Figure 6-21: Comparison of ϕ profiles for baseline case (blue) and case 4 (red). The weak rotor hub leads to a large (70% of span) stall cell developing at $\Phi = .709$.

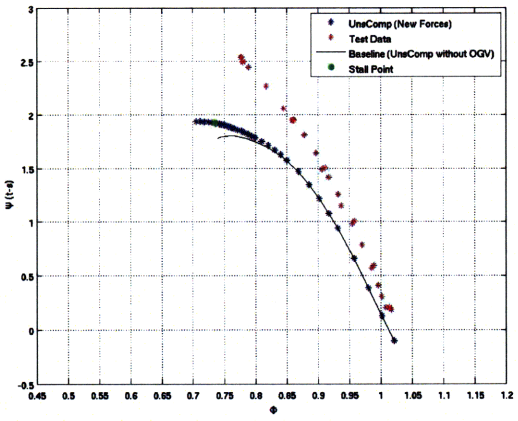

(a) Overall characteristics

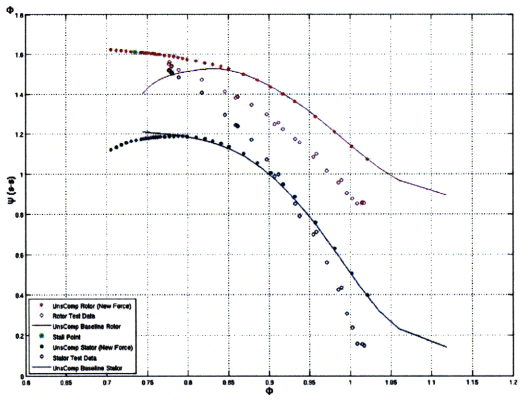

(b) Blade characteristics

Figure 6-22: Comparison of characteristics for case 5 to baseline case and test data. The computed stall point is marked in green.

6-23(a)) before the stall cell fully develops, longer than the 3 or so revolutions found in previous work (1). This behavior is similar to the baseline and in contrast to case 2 where the stall cell develops in 1-2 rotor revolutions. The stall point for this case is $\Phi = .734$, 4% below the baseline.

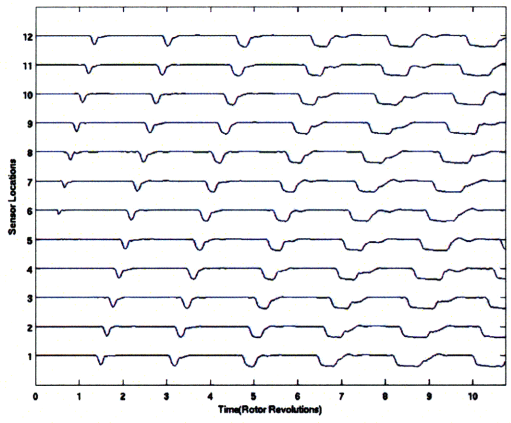

(a) ϕ traces at the rotor tip $\Phi = .734$

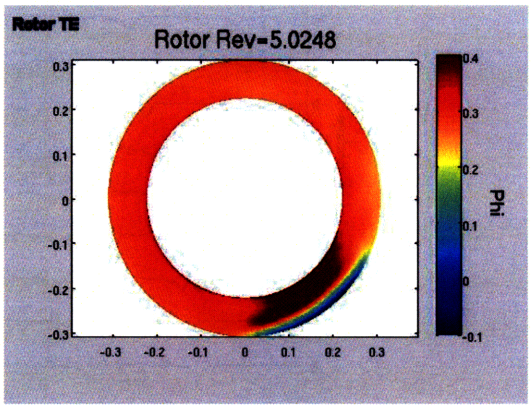

(b) Developing stall cell

Figure 6-23: Spike takes 6-7 revolutions to fully develop into a stall cell.

The pressure rise in case 6, with an increase of tangential force at the tip of the rotor, is similar to case 3 and to the baseline case, as seen in 6-24. The maximum difference between the overall characteristics is 1% for case 6 and the baseline. However, the traces in Figure 6-25 (case 6) do not show modes, in contrast to case 3, and the development of the spike

into a stall cell occurs at 6-7 revolutions, similar to case 5.

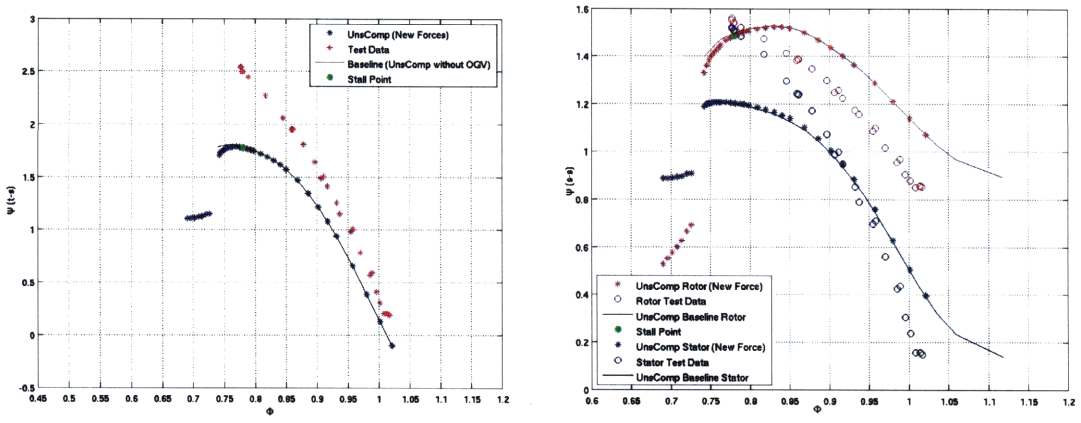

(a) Overall characteristics

(b) Blade characteristics

Figure 6-24: Comparison of characteristics for case 6 to baseline case and test data. The computed stall point is marked in green. Characteristics for this case are nearly identical to baseline case.

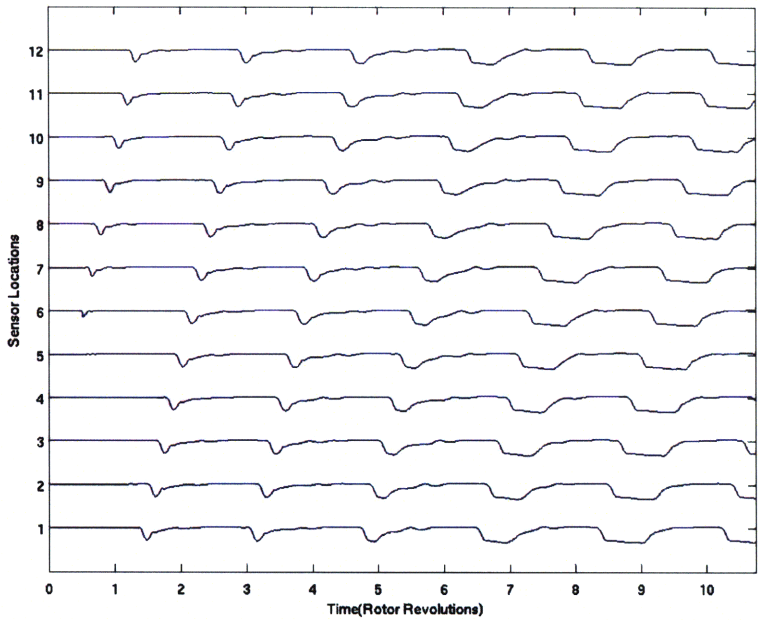

Figure 6-25: ϕ traces at the rotor tip $\Phi = .78$. The stall inception type is spike.

A summary of results for cases 4-6 is given in Table 6.4. The key results are (1) cases 2 and 5 show that the stall inception type was more sensitive to axial force at the tip than at the hub, (2) reduction of axial force at the hub can lead to modal stall at that location, (3)

increasing the tangential force at the tip eliminated the formation of modes (case 6), and (4) the stall point was sensitive to changes in the axial force but not changes in tangential force.

Case Number	Φ_{stall}	Inception Type	Final Form
Case 4	$\Phi = .709$	Modal	Part Span (70% of span)
Case 5	$\Phi = .734$	Spike (slow)	Part Span
Case 6	$\Phi = .78$	Spike (slow)	Part Span

Table 6.4: Summary of result at the rotor Hub. "Spike (slow)" refers to spike developing slower than expected.

6.3.2 Axial Distribution

To assess effects of the axial distribution two different distributions (other than the baseline) were examined. There was a parabolic distribution and a trailing edge-loaded exponential distribution, as listed in Table 6.5. Example distributions are shown in Figure 6-26. The total force along a given streamline was kept the same as in the baseline case. The same shape distribution was used for each streamline.

Case Number	Description
Case 7	Parabolic Distribution
Case 8	Exponential Distribution

Table 6.5: List of cases for the axial distribution section of the sensitivity analysis.

In the baseline case, all the distributions were leading edge loaded and roughly exponentials. (Baseline rotor distributions were shown in Figure 3-9 and 3-10). The exponential distribution in case 8 was selected to represent the force in a region of reversed flow. The parabolic distribution was selected as a "middle ground" between the baseline and the trailing edge loaded distributions.

The characteristics for case 7 and 8 are shown in Figure 6-27. In case 7 there are discontinuities in the axisymmetric characteristic near the stall point. The stall point is located just before the discontinuity at $\Phi = .736$, 5% lower that the stall point in the baseline case. It is not clear why this discontinuity arises. The discontinuity may occur because of the situation shown in Figure 4-10 or it may be related to the fact that the

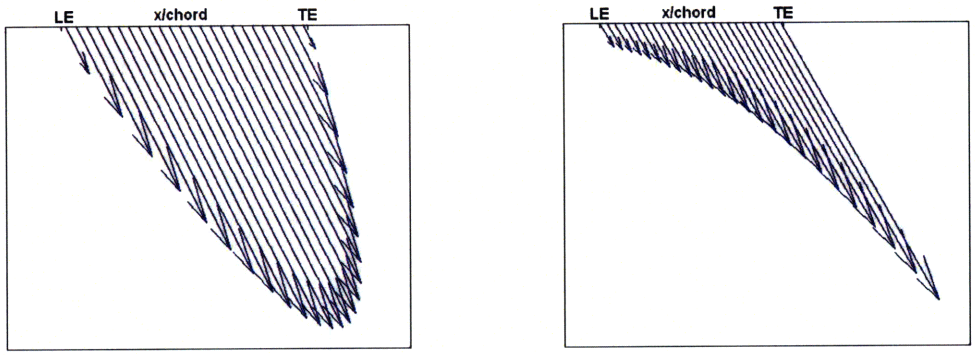

(a) (b)

Figure 6-26: Examples of parabolic distribution (a) and exponential distribution (b). Along the span, these are scaled to match the total force at that spanwise location give by the 2D/SLC database.

distribution does not vary along the span.

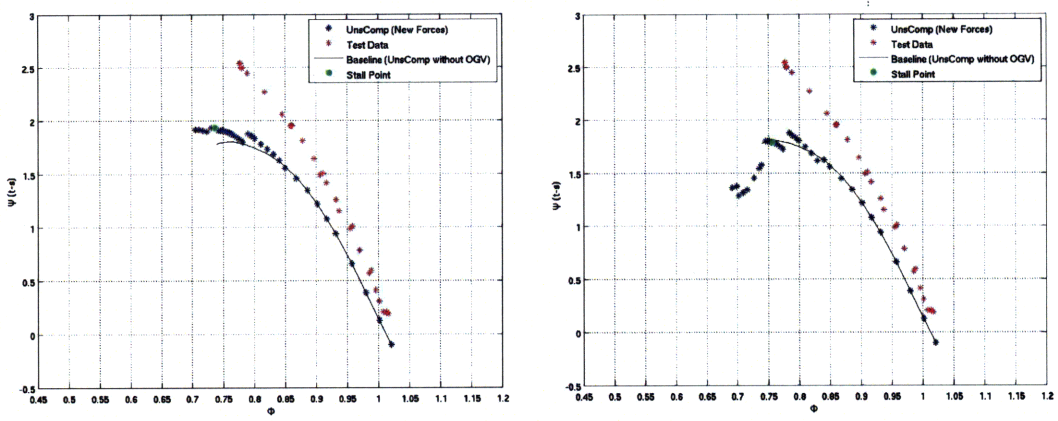

(a) Overall characteristics (b) Blade characteristics

Figure 6-27: Comparison of characteristics for case 7 to baseline case and test data. The computed stall point is marked in green. Change in distribution causes a discontinuity in the characteristic.

In case 7, the stall inception type seems to be modal and the stall cell grows in the stator hub (Figure 6-28). The input spike decays, the apparent mode develops at the stator hub, and begins rotating at 30% of rotor speed. From Figure 6-29(a), there is a reduced velocity in the rotor hub that leads to stator hub separation, and compared to case 4, the stator hub is weaker for case 7. This may be the reason why the stall cell grows in the stator.

Case 8 shows modes growing in the rotor hub rather than in the stator hub, likely due

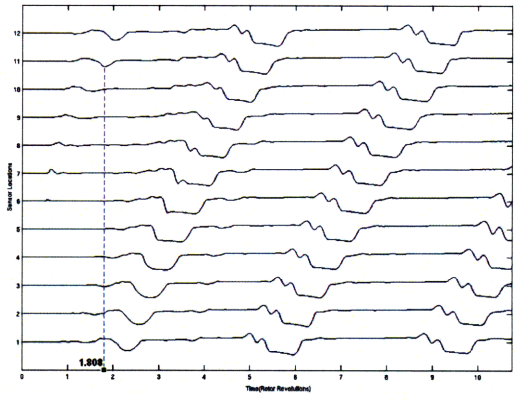

(a) ϕ traces at the rotor hub $\Phi = .736$

(b) ϕ traces at the stator hub $\Phi = .736$

Figure 6-28: Modes develop into a stall cell originating from the stator hub. Time when the modes begin to grow is noted on each plot.

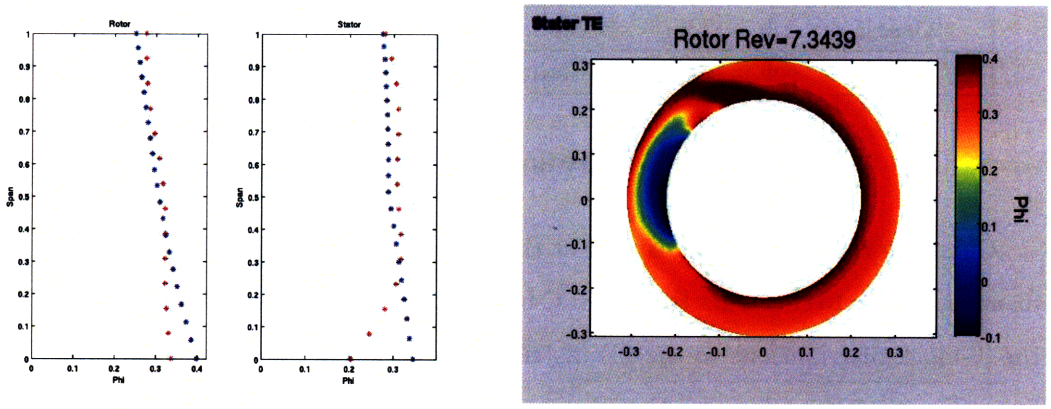

(a) Rotor and Stator ϕ profiles

(b) Stall cell at the Stator Hub

Figure 6-29: Comparison of ϕ profiles for baseline case (blue) and case 4 (red). Weak stator hub (in response to rotor hub flow) leads to the large (70% of span) stall cell developing at this point.

to the fact that the stator hub is stronger in case 8 (Figure 6-30(a)) than in case 7. Two part span stall cells develop (Figure 6-30(b)).

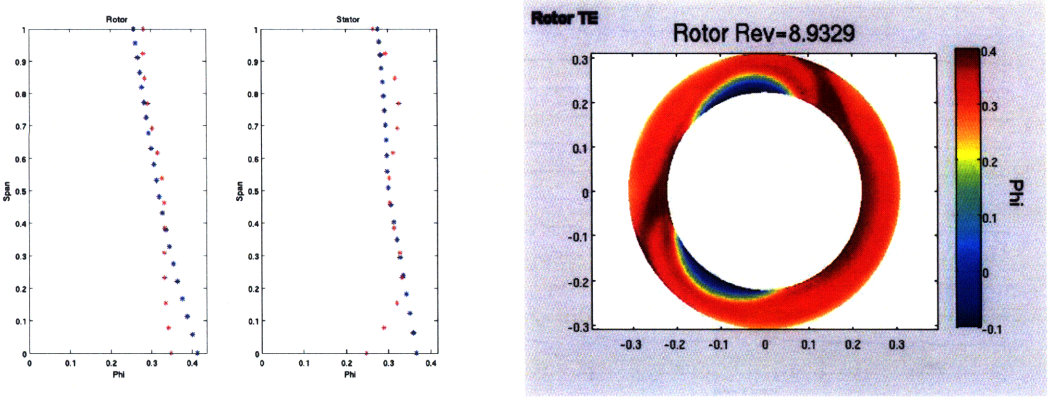

(a) Rotor and Stator ϕ profiles

(b) Stall cell at the Stator Hub

Figure 6-30: Comparison of ϕ profiles for baseline case (blue) and case 4 (red). Weakened rotor hub leads to two part span (50% of span) stall cells at this point.

A summary of results for cases 7 and 8 is found in Table 6.6. Key results are: (1) the axial distribution can affect the stalling behavior but (2) the stall point was only mildly sensitive to the change in distribution (maximum 5% change in stall point).

Case Number	Φ_{stall}	Inception Type	Final Form
Case 7	$\Phi = .736$	Modal	Part Span (70% of span)
Case 8	$\Phi = .756$	Modal	Two Part Span cells (50% of span)

Table 6.6: Summary of results for axial distributions.

Changing the distribution of force at the peak of the characteristic is part of the attachment procedure to construct the 3D/SLC body force database (Section 2.5). Switching from the T-block distributions to the 2D distributions gives rise to a discontinuity in the local force (Figure 4-10). The situation shown in that figure occurs in cases 7 and 8. Although the results from these two cases do not completely describe the effects of changing the axial force distribution, they raise the question of which distributions should be used past the stall point: 2D distributions (2D/SLC model) or the last T-block distribution (Kiwada(8))?

6.3.3 Force and Overall Flow Coefficient

Gong(5) studied the effect on stall point and type of changing the characteristic below the peak. The body forces were generated from the five characteristics shown in Figure 6-31 and following the original procedure developed by Gong(4). The baseline case was the test data characteristic which is labeled "C" in the figure. The incompressible version of UnsComp was used.

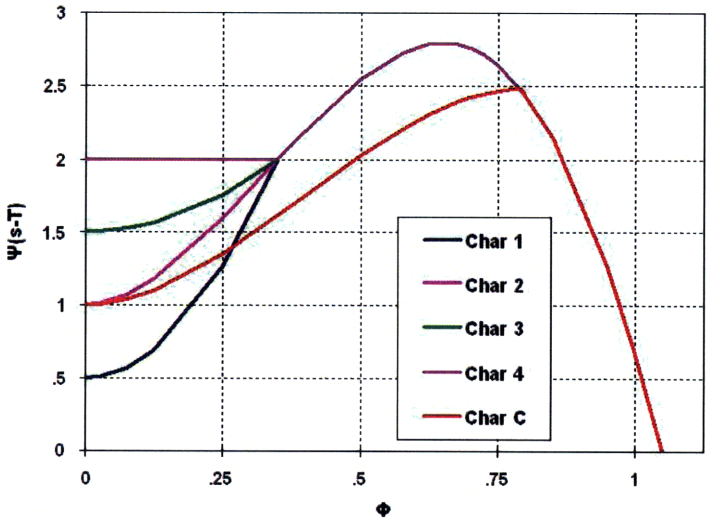

Figure 6-31: Five different characteristics generated by Gong. Characteristic C is from the experimental data.

The results are shown in Table 6.7. The first column gives the value of Φ for which a spike is sustained but does not grow into a stall cell (behavior not seen in the experiments). The third column shows Φ_{stall}. The second and forth columns compare these flow coefficients to the measured stalling coefficient($\Phi_{stall_{test}} = .78$). The conclusion is that the stall inception type, and the final form of the instability, are not sensitive to changes in the characteristic at low flow. The stall point is sensitive showing a change of 5.6% for Char 3.

The link between the sensitivity of the characteristic and the sensitivity of the force is not immediately clear since the body force databases were not generated from the 2D/SLC model. Shown in Figure 6-32, the characteristic from the baseline case (with OGV) is compared to "Char 4" from Gong's incompressible analysis. The pressure rise is lower for the UnsComp characteristic but the behavior is qualitatively similar. From Section 6.2.2,

Char	Φ_{spike}	$\frac{\Phi_{spike}-\Phi_{test}}{\Phi_{test}}$	Φ_{stall}	$\frac{\Phi_{stall}-\Phi_{test}}{\Phi_{test}}$	Final form
1	.842	8%	.803	3%	Ring
2	.842	8%	.788	1%	Ring
3	.842	8%	.783	4%	Ring
4	.842	8%	.765	-2%	Ring
5	.858	10%	.821	5.2%	Ring

Table 6.7: Results of the assessment to the sensitivity of the stall point, stall inception type, and final form to changes in the characteristic at low flow(5).

the results were that $\Phi_{stall} = .776$, the stall inception was spike, and the final form part-span rotating stall. These results are similar (1.4% difference) to the results shown in Table 6.7 for "Char 4". This was the only case where the computed the stall point was lower than the experiment. That same behavior is found in the baseline calculations (6.2.2). This comparison suggest that the results are applicable to stability analysis using the 2D/SLC body force database.

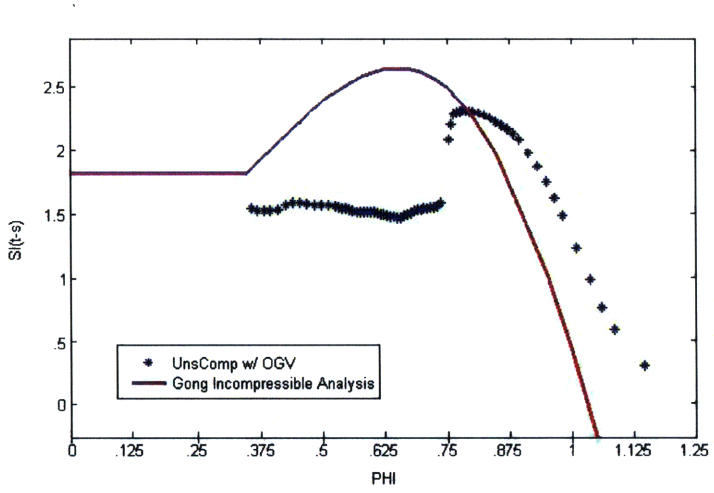

Figure 6-32: Comparison of the characteristic computed from the current set of body force (UnsComp w/ OGV) and characteristic 4.

6.4 Summary

The results show that axial force at the tip of the rotor is the most important parameter that affecting the stall point and stall inception type. This suggests that a tip leakage model

should be implemented into the 2D/SLC model. The axial force distribution is of secondary importance. Although the assessment suggest that it can affect the stall inception type, there is not enough data to determine how sensitive the stall point and type are to the force distribution. Finally, the unsteady behavior was sensitive to the tangential force in the tip region and it was observed that increasing the tangential force eliminated the modes.

Chapter 7

Summary and Conclusions, and Future Work

7.1 Summary

In this thesis a compressor body force database was developed to be used in a stall prediction methodology based on forces extracted from flow fields computed by two and three dimensional Navier-Stokes solvers and streamline curvature methods. A stability analysis using this database was shown to capture the qualitative features of stall and inception observed in the experimental data. An assessment of the sensitivity of stall point and stall inception type to the form of body force at flows below the peak of the characteristic was presented.

Chapter 1 reviewed compressor instability, the two stall inception types (spike and modes), the concept of the body force, and summarized features of the Euler code used for the stability analysis.

Chapter 2 described the 2D/SLC model and the methodology used to develop the body body force database. including (1) calculation of the two-dimensional flow field from design to low flow, (2) a streamline curvature calculation using the loss and deviation computed from the 2D flow field, and (3) developing the axial distribution of body force from leading to trailing edge.

Chapter 3 described details of the 2D calculation including (1) loss and deviations computed from the solution and (2) the procedure for calculating the chordwise distribution

of body force.

Chapter 4 described the SLC procedure which used the computed loss and deviations to calculate the axisymmetric flow field and the body force database. The steps included (1) extraction, of the body force from the flow field and (2) distribution of this body force along the chord using the 2D chordwise distributions. The procedure to join the body force computed from SLC to force computed from T-block is also presented.

In Chapter 5, an assessment of the self-consistency of the stall prediction methodology is offered using the 2D/SLC body force database developed in Chapter 4. Three aspects are covered: (1) the body force input, (2) the Euler code, UnsComp, and (3) the axisymmetric flow field.

Chapter 6 presents a sensitivity assessment of the stall point and inception type to three parameters: F_x, F_t, and $f(x)$.

7.2 Conclusions

1. For the parameters studied, the stall point is most sensitive to the axial force. Reducing the axial force by 30% at the tip results in a decrease of the stall flow by 15% for the compressor examined.

2. The stall inception type (modes versus spikes) is sensitive to the axial force at the tip and the chordwise force distribution. Reducing the axial force led to spike stall and the more trailing edge loaded distributions led to modal stall.

3. The computed location at which the stall cell developed was sensitive to the axial force and the chordwise distribution of force.

4. The order of importance of the features of the body force past the peak, on stall onset, are: spanwise distribution axial force, chordwise force distribution, and spanwise distribution tangential force at the rotor tip.

7.3 Recommendations for Future Work

This thesis is one part of a ongoing project and the following work is of immediate interest to determine which specific flow effects must be incorporated into the body force representation for the compressor for an accurate stall onset prediction

1. Develop a sensitivity analysis using the 3D/SLC body force database. This database captures the effects of tip leakage near the peak of the characteristic. The work would supplement the sensitivity assessment by determining the effect of tip clearance before the stall point has on stability.

2. Develop and implement a body force representation that incorporates effects of tip leakage flow which impact stall onset. This can be done through several means, for example, modeling these effects in throughflow calculations.

3. Extend the sensitivity assessment of stall onset to body force distribution using the 3D/SLC body force database. The assessment should attempt to determine the importance of shape of the characteristic, force in the tip region, and the input disturbance.

4. Link the axial force distribution to the axisymmetric flow field to enable insight of how the body forces are related to pressure rise and velocity profiles. This work is prompted by the response of the axisymmetric flow to the change in distribution seen in the sensitivity assessment.

Appendix A

Detailed Body Force Description

A.1 Governing Equations

From Greitzer et al(6), below are the steady Navier Stokes equations in cylindrical coordinates. The notation is the same as commonly used and $\underline{\underline{\tau}}$ is the stress tensor. The forces (F_x, F_θ, F_r) are any external body force. Ignoring gravitational effects, this becomes the blade body force. If the flow field is known throughout the domain the body force can be calculated from these equations(8).

$$\frac{1}{r}\frac{\partial V_r V_x}{\partial r} + \frac{1}{r}\frac{\partial V_\theta V_x}{\partial \theta} + \frac{\partial V_x^2}{\partial x} = -\frac{1}{\rho}\frac{\partial P}{\partial x} + \hat{x}\cdot\nabla\underline{\underline{\tau}} + F_x \tag{A.1}$$

$$\frac{1}{r}\frac{\partial V_r V_\theta r}{\partial r} + \frac{1}{r}\frac{\partial V_\theta^2}{\partial \theta} + \frac{\partial V_\theta V_x}{\partial x} + \frac{V_x V_\theta}{r} = -\frac{1}{r\rho}\frac{\partial P}{\partial \theta} + \hat{\theta}\cdot\nabla\underline{\underline{\tau}} - \frac{\Omega V_r}{r} + F_\theta \tag{A.2}$$

$$\frac{1}{r}\frac{\partial V_r^2 r}{\partial r} + \frac{1}{r}\frac{\partial V_r V_\theta}{\partial \theta} + \frac{\partial V_r V_x}{\partial x} - \frac{V_\theta^2}{r} = -\frac{1}{\rho}\frac{\partial P}{\partial r} + \hat{r}\cdot\nabla\underline{\underline{\tau}} + \frac{\Omega V_\theta}{r} + \frac{\Omega^2}{r^2} + F_r \tag{A.3}$$

A.2 Body Force Formulation

The body force formulation is based on the conservative form of Eqns. A.1 -A.3. This can be expressed in terms of the components of mass and momentum flux (Eqn. 1.1). This is the body force description developed by Gong(4). Kiwada(8) developed the "blade force" averaging procedure which averages these flux terms in the theta direction. These are (A.4-A.7) the equations in the body force model.

$$F = \begin{bmatrix} r\rho V_x \\ r\rho V_x^2 + rP \\ r\rho V_x r V_\theta \\ r\rho V_x V_r \end{bmatrix} b \tag{A.4}$$

$$G = \begin{bmatrix} r\rho V_\theta \\ r\rho V_x V_\theta \\ r\rho V_\theta^2 + rP \\ r\rho V_r V_\theta \end{bmatrix} b \tag{A.5}$$

$$H = \begin{bmatrix} r\rho V_r \\ r\rho V_x V_r \\ r\rho V_r r V_\theta \\ r\rho V_r^2 + rP \end{bmatrix} b \tag{A.6}$$

$$S = \begin{bmatrix} 0 \\ br\rho F_x + rP\frac{\partial b}{\partial x} \\ br\rho r F_\theta + rP\frac{\partial b}{\partial \theta} \\ b\rho V_\theta^2 + bP + br\rho F_r + rP\frac{\partial b}{\partial r} \end{bmatrix} \tag{A.7}$$

Appendix B

Assembly Procedure

The flow over each blade row in the compressor was computed separately and allowed to mix out to avoid the need for mixing planes. The output from the 2D calculation gives us the loss and deviation as a function of incidence for each blade row which is used to link the blade rows (Figure 3-6-3-8). The result of this process is the characteristics at each of the three radii and more importantly the local dynamic head seen by each of the blades.

The axial velocity is constant throughout the compressor. This is true for a 2D calculation which can be thought of as a flow along a streamline in the axisymmetric plane with $\delta radius = 0$ (i.e. no streamline curvature). For that process, from conservation of mass, V_x is constant.

$$\dot{m} = \rho V_x A \tag{B.1}$$

The inlet tangential velocity is determined by the relative velocity at the trailing edge of the previous blade. The inlet flow angle can be calculated using the two components of velocity.

$$\alpha_1 = tan^{-1}(\frac{V_y}{V_x}) \tag{B.2}$$

Assuming you know the camber angle θ_1, the incidence can be calculated. The computed curves are interpolated to find the loss and deviation. After computing the deviation the exit flow angle is given by the difference between the deviation and exit camber angle. The exit tangential velocity is then determined by solving Eqn. B.2 for V_y.

Bernoulli's equation applies on along streamline for steady, incompressible flow. The static pressure is known from the downstream condition of the previous blade row.

$$P_{t_1} = P_1 + \frac{1}{2}\rho V_1^2 \tag{B.3}$$

After calculating the magnitude of the velocity vector the total pressure upstream of the blade can be computed. The total pressure after the blade row is calculated using Eqn. B.4. The static pressure can be calculated using Eqn. B.3 solved for the exit P.

$$P_{t_2} = P_{t_1} - \frac{1}{2}\omega\rho V_2^2 \tag{B.4}$$

B.1 Local Dynamic Head

The local dynamic head, q, refers to $\frac{1}{2}\rho V^2$ where V is the velocity at the leading edge of any of the four blade rows. This variable is needed for calculating the force distribution along the blade. The 2D calculations were run fixing a V_y and then varying the V_x to change the incidence angle. However, there is no reason that the selected V_y will be in the same as the actual V_y calculated by assembling the blades. The incidence angle is one variable that determines the flow field, however, the magnitude of the flow variables scale with the local dynamic head. Ignoring the effects of Reynolds number, this is the only other variable needed to uniquely determine the flow field (7). To correct for the difference local dynamic head all the flow variables were scaled before the distribution body force was extracted. As an example, the way the pressure from the 2D calculation was modified is shown in Eqn. B.5

$$P_{actual} = P_{2D}(\frac{q_{actual}}{q_{2D}}) \tag{B.5}$$

B.2 Assembly Results

The results of that process are the characteristics at each of the radius where the 2D calculation was run. These are not needed for the body force extraction as per the 2D/SLC model, but were useful in evaluating this process. Those characteristic are shown in Figure B-1.

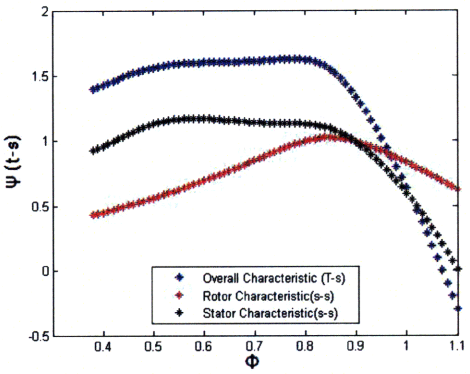

(a) Hub Characteristics

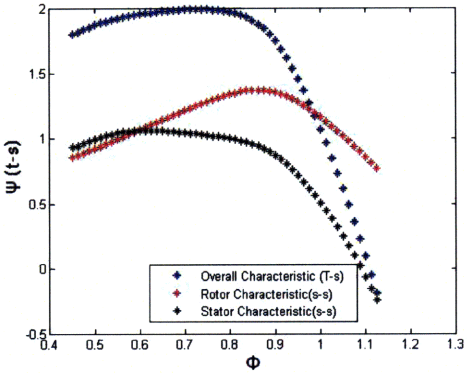

(b) Mean Characteristics

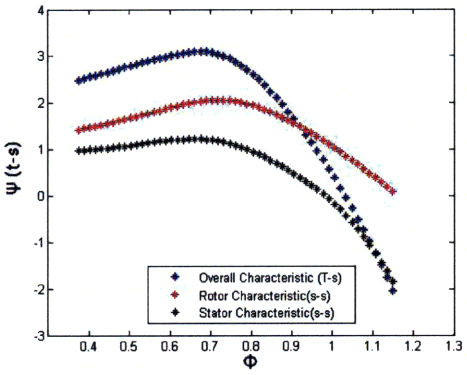

(c) Tip Characteristics

Figure B-1: Hub, mean, and tip characteristics. Plotted are the overall $\psi(t-s)$ curves as well as the blade $\psi(s-s)$ curves. The abscissa contains the values of ϕ_{local} the reason for the large values of "phi" at the hub when compared to the tip.

Appendix C

2D and SLC Calculation Assessments

C.1 2D Assessment

Two parts of this calculation need to be assessed, the loss and deviation from the 2D computation and the characteristic computed after assembling. The former is to show that the 2D FLUENT calculations were run correctly. The latter shows that the data was processed correctly. These results have already been qualitatively verified, but a more quantitative assesment is offered.

To verify the 2D calculation, the loss and deviation are compared to the results obtained from Carter's rule and the diffusion factor-loss correlation. These correlations are only valid before the stall point and thus the assessment only includes flow coefficients near design. The loss and deviation cannot be assessed past the peak of the characteristic.

Carter's Rule only gives a value of deviation corresponding to minimum-loss incidence, although, before stall deviation is only a weak function of incidence(2). Table C.1 shows

Φ	i°	2D δ	Carter δ
1	-0.89	3.50	3.72
.904	3.08	4.76	3.72
.809	6.90	7.56	3.72

Table C.1: Computed deviation compared to deviation from Carter's Rule at three flow coefficients.

ϕ	i°	2D DF	2D Loss	DF Correlation Loss
.1	-0.89	.3411	0.0391	0.0437
.904	3.08	.4420	0.0618	0.0625
.809	6.90	.5081	0.1118	0.1188

Table C.2: Computed loss compared to loss from the DF-loss correlation at three flow coefficients.

that the deviations computed from the 2D calculation and Carter's Rule are within 5% near design.

The loss, ω, is another indicator of the applicability of the solution. Loss can be correlated to the diffusion factor through the blade angles, β (Eqn. C.1 (7)).

$$\omega \left(\frac{cos(\beta_2)}{\sigma} \right) \left(\frac{cos(\beta_2)}{cos(\beta_1)} \right)^2 = f(DF) \tag{C.1}$$

Where $F(DF)$ can be read from a plot found in the standard literature. Table C.1 gives the loss from the 2D calculation and the loss from the correlation. Given this and the results from Table C.1, the conclusion is that the results from the 2D calculation are reasonable.

The second step is to validate the assembly process. This was done independently by Li(9) using the loss and and deviation from the 2D calculation and a one-dimensional velocity vector analysis. In Figure C-1. The results match well for the entire range. From this, the conclusion is that the assembly procedure is correct and the local dynamic head calculated from this procedure is also correct.

C.2 SLC Assessment

The MIT SLC solution must be assessed before the body force can be extracted. This was done by comparing the solution with hub to tip ratio of .99 at 10%, 50%, and 90% span to the characteristics from the 2D calculation. Since the loss and deviations from the 2D calculation were used as inputs for MIT SLC, if the SLC calculation was run correctly the characteristics should line up. In Figure C-2 this is shown to be the case.

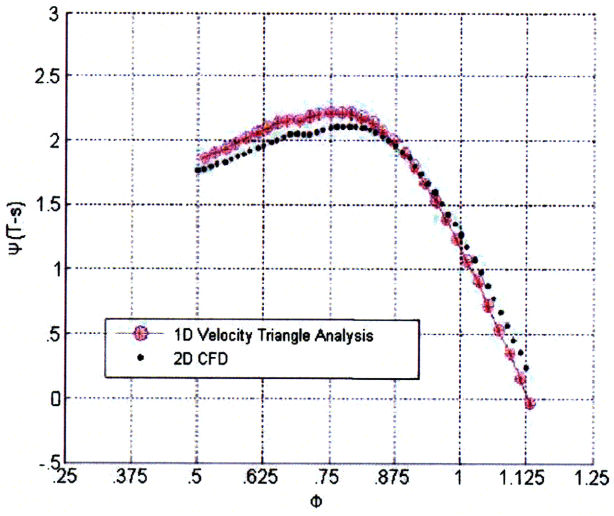

Figure C-1: Comparison of computed 2D characteristic at the meanline a characteristic generated using a one-dimensional velocity triangles analysis.

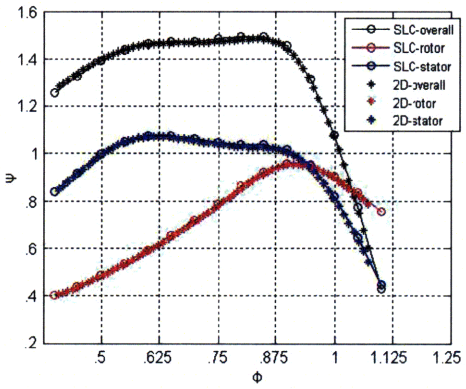

(a) Hub Characteristics Comparison

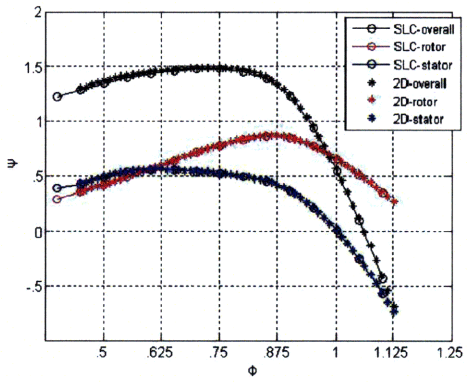

(b) Mean Characteristics Comparison

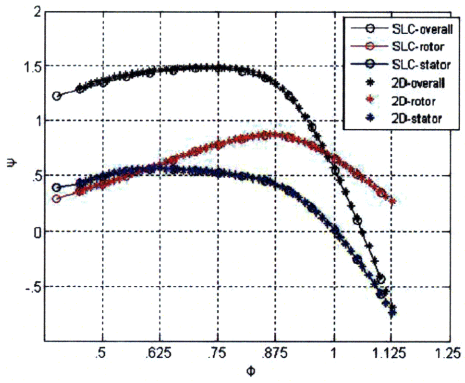

(c) Tip Characteristics Comparison

Figure C-2: Hub, mean, and tip characteristics. Plotted are the overall $\psi(t-s)$ curve as well as the blade $\psi(s-s)$ curves. Comparison shows that the SLC high H-T ratio and the 2D curves match exactly(9).

References

[1] CAMP, T., AND DAY, I. A Study of Spike and Modal Stall Phenomena in a Low-Speed Axial Compressor. *Journal of Turbomachinery 120* (July 1998), 393–401.

[2] CUMPSTY, N. *Compressor Aerodynamics.* Krieger Publishing Company, 2004.

[3] DENTON, J. personal communication, 2007.

[4] GONG, Y. *A Computational Model for Rotating Stall and Inlet Distortions in Multistage Compressors.* PhD thesis, Massachusetts Institute of Technology, Dept. of Aeronautics And Astronautics, February 1999.

[5] GONG, Y. personal communication, 2008.

[6] GREITZER, E., TAN, C., AND GRAF, M. *Internal Flow Concepts and Applications.* Cambridge University Press, 2004.

[7] KERREBROCK, J. L. *Aircraft Engines and Gas Turbines.* The MIT Press, 1992.

[8] KIWADA, G. Development of a Body Force Description for Compressor Stability Assessment. Master's thesis, Massachusetts Institute of Technology, Dept. of Aeronautics And Astronautics, February 2008.

[9] LI, Q. personal communication, 2008.

[10] LONGLEY, J. P. Calculating the Flow Field Behavior of High-Speed Multi-stage Compressors. In *ASME* (June 1997), no. 97-GT-468.

[11] PATEL, A. personal communication, 2008.

[12] XU, L. Assesing Viscous Body Forces for Unsteady Calculations. *Journal of Turbomachinery 125* (July 2003), 425–432.

[13] XU, L., HYNES, T., AND DENTON, J. Towards Long Length Scale Unsteady Modeling in Turbomachines. *Proc. Instn Mech. Engrs 217 Part A:J. Power and Energy* (October 2002), 75–82.